



Enhanced electrocatalytic cathodic degradation of 2,4-dichlorophenoxyacetic acid based on a synergistic effect obtained from Co single atoms and Cu nanoclusters

Lu Liu^a, Yiran Chen^a, Shunlin Li^a, Wenchao Yu^a, Xinyu Zhang^a, Hui Wang^{a,*}, Jianan Ren^a, Zhaoyong Bian^{b,**}

^a College of Environmental Science and Engineering, Beijing Forestry University, Beijing 100083, PR China

^b College of Water Sciences, Beijing Normal University, Beijing 100875, PR China

ARTICLE INFO

Keywords:

Dual active sites

Dual function

Chlorinated organic pollutant

Degradation mechanism

ABSTRACT

Electrochemical reduction-oxidation is an environmentally-friendly process of degrading 2,4-dichlorophenoxyacetic acid (2,4-D). However, the design of electrocatalysts having reductive dechlorination and oxygen-specific active sites remains challenging. In the present study, catalytic cathodes were made from single Co atoms and Cu nanoclusters on nitrogen-doped carbon to enhance the degradation of 2,4-D through a synergistic mechanism. In this process, 2,4-D was dechlorinated on the Cu nanoclusters and then oxidized by $\cdot\text{OH}$ radicals produced by the conversion of O_2 on the Co atoms. The Cu nanoclusters served as both conductive bridges and 2,4-D adsorption sites to improve the electron transfer of the circuit and so accelerate the direct electron transfer associated with dechlorination. The single Co atoms first reduced O_2 to H_2O_2 and then continuously catalyzed the decomposition of this H_2O_2 to form $\cdot\text{OH}$. As a result of the synergistic combination of these two effects, complete efficient dechlorination and 93.4% total organic carbon removal were achieved after 2 h. The kinetics constant for this reaction was determined to be $546.4 \text{ min}^{-1} \cdot \text{g}_{\text{metal}}^{-1}$, indicating exceptional performance relative to previous reports of organic pollutant degradation. This study demonstrates the rational design of a bifunctional electrocatalyst and elucidates the electron transfer pathway and O_2 activation mechanism associated with 2,4-D removal by electrochemical reduction-oxidation. This process is likely to have potential applications in the remediation of polluted water.

1. Introduction

2,4-Dichlorophenoxyacetic acid (2,4-D) is a chlorinated phenoxy herbicide widely used in weed control [1]. At present, more than 1500 herbicide products worldwide contain 2,4-D as an active ingredient [2, 3]. Because this compound is highly soluble in water and exhibits poor biodegradability it is listed as a potential groundwater contaminant by the United States Environmental Protection Agency [4,5]. In recent decades, a variety of processes for the effective removal of chlorinated organic pollutants from water have been developed, including those based on electrocatalysis, photo-Fenton processes, photo-electrocatalysis, combined electrochemical and biological treatments, photocatalysis combined with biological treatments, and

Fenton-like reactions in conjunction with persulfate activation processes [6–18].

Electrochemical reductive dechlorination can effectively remove chlorine atoms from chlorinated organic pollutants and reduce pollutant toxicity, which has been reported in many articles [19–25]. However, electrochemical reductive dechlorination process does not further degrade dechlorination intermediates, and these intermediates are not biodegradable. Advanced oxidation processes based on hydroxyl radicals are also widely used for the degradation of POPs, but may produce oxidation intermediates that are more toxic than the original contaminants [26–28]. The coupling of electrocatalytic reductive dechlorination and oxidative degradation reactions can integrate the advantages of both processes, which improve the degradation efficiency of chlorinated

* Correspondence to: College of Environmental Science and Engineering, Beijing Forestry University, No. 35 Qinghua East Road, Haidian District, Beijing 100083, PR China.

** Correspondence to: College of Water Sciences, Beijing Normal University, No. 19 Xijiekouwai Street, Haidian District, Beijing 100875, PR China.

E-mail addresses: wanghui@bjfu.edu.cn (H. Wang), bian@bnu.edu.cn (Z. Bian).

<https://doi.org/10.1016/j.apcatb.2023.122748>

Received 30 December 2022; Received in revised form 5 April 2023; Accepted 8 April 2023

Available online 10 April 2023

0926-3373/© 2023 Elsevier B.V. All rights reserved.

organic pollutants. Therefore, it is very useful and urgent to improve the degradation efficiency of pollutants through reductive dechlorination and oxidation reactions.

Electrocatalytic reduction-oxidation systems offer a means of efficiently remediating pollution with organic compounds. In these processes, chlorinated organic pollutants are completely dechlorinated and mineralized by reduction-oxidation-mediated electro-Fenton processes, employing a composite cathode for dechlorination and to facilitate the $2e^-$ oxygen reduction reaction (ORR) and the $1e^-$ reaction of H_2O_2 to produce $\cdot OH$ radicals [27,29]. In situ generation of H_2O_2 by heterogeneous electro-Fenton reaction is an environmentally friendly and economical method for the efficient generation of $\cdot OH$ radicals [30]. Although Fe doping can rapidly activate H_2O_2 , it leads to a $4e^-$ ORR [12, 26]. The activity and selectivity of monoatomic catalysts can also be adjusted by changing the metal center and coordination environment as a result of the unique electronic structures and unsaturated coordination of these centers [31,32]. Work involving theoretical calculations and experiments has demonstrated the relative rates for the electrochemical production of H_2O_2 over a series of M-N-C materials (M = Mn, Fe, Co, Ni or C), and Co-N-C catalysts have been shown to provide the highest H_2O_2 yields [33]. Co-based catalysts also exhibit the ability to readily decompose H_2O_2 and so have potential as heterogeneous Fenton-like catalysts [34–36].

Noble metal catalysts are widely used in electrocatalytic hydrodechlorination but the use of these elements greatly increases the cost of the reduction-oxidation process [37–40]. For this reason, Cu has been considered as a substitute for precious metals in electroreduction dechlorination systems. As an example, a modified Cu foam electrode was found to promote dechlorination via a reduction pathway involving direct electron transfer [41,42].

In a reduction-oxidation system, pollutants can be quickly adsorbed on the cathode surface and reduced, which is crucial for the electrocatalytic reduction of 2,4-D dechlorination. At the same time, the cathode catalyst also needs to generate H_2O_2 in situ by O_2 reduction reaction and activate H_2O_2 to $\cdot OH$, which is used to oxidize the dechlorination intermediates. To achieve reductive dechlorination and oxidative degradation of 2,4-D, the co-existence of clusters for reductive dechlorination and single atoms for $\cdot OH$ production has great potential to optimize the catalytic performance. Therefore, bifunctional coupling sites of Cu clusters (Cu_p) and single-atom Co (Co_{SA}) were designed to enhance the reductive dechlorination and oxidative degradation, respectively. Currently, nanocluster and single atomic coupling catalysts have not been investigated for electroreductive dechlorination and degradation of pollutants by converting O_2 to $\cdot OH$ via $(2+1)e^-$ process.

On this basis, the present work designed and fabricated a combination of single Co atoms and Cu nanoclusters deposited on nitrogen-doped carbon ($Co_1Cu_p\text{-NC}$). This material was found to enhance the degradation of chlorinated persistent organic pollutants in water via an electrocatalytic reduction-oxidation process. A $Co_1Cu_p\text{-NC}$ catalytic cathode was prepared and various quenching reactions were performed in conjunction with analyses by electron paramagnetic resonance (EPR) spectroscopy to identify reactive oxygen species (ROS). The reductive dechlorination ability of this material was also demonstrated using electrochemical experiments. The 2,4-D adsorption capacity, electron transfer ability and free radical generation mechanism occurring at key active sites were all evaluated using density functional theory (DFT) calculations. A possible mechanism for the degradation of 2,4-D was elucidated based on the experimental data and theoretical analysis.

2. Materials and methods

2.1. Synthesis of $Co_1Cu_p\text{-NC}$

Synthesis of $Co_{SA}\text{-NC}$: This material was produced using an improved version of a previously published method [43]. In a typical process, melamine, carbon black and cobaltous acetate tetrahydrate were ground

and thoroughly mixed, after which ethanol was added to the mixture and the materials were further ground in a fume hood until all the ethanol had evaporated. The resulting solid mixture was dried in an oven at 60°C and then ground again. The mixture was then transferred into a tube furnace and heated to 600°C at a rate of $2.5^\circ\text{C}\cdot\text{min}^{-1}$ under Ar, annealed at that temperature for 2 h, then heated to 900°C at $5^\circ\text{C}\cdot\text{min}^{-1}$ and annealed at that higher temperature for 90 min. The black solid resulting from this process was ground and acid etched to remove metal clusters, giving the $Co_{SA}\text{-NC}$ catalyst. The catalyst without metal doping is denoted as NC.

Synthesis of $Co_1Cu_p\text{-NC}$: This material was prepared using an improved version of the method reported by Song et al. [44], as summarized in Fig. 1a. In a typical synthesis reaction, 150 mL N, N-dimethylformamide was transferred into a 500 mL flask and heated in an oil bath at 140°C . Following this, a copper nitrate solution was slowly added to the solvent after which the solution was refluxed for 12 h. After this, a 150 mg quantity of the $Co_{SA}\text{-NC}$ was ultrasonically dispersed in 200 mL of deionized water after which the Cu precursor solution was slowly added to the dispersion followed by stirring at room temperature for 90 min. Slowly add the reducing agent $NaBH_4$ dropwise. This was followed by stirring for 12 h. The $Co_1Cu_p\text{-NC}$ was obtained after filtration, washing, and freeze-drying of the resulting suspension. In a separate synthesis, $Cu_p\text{-NC}$ was also produced. Text S1 provides additional details concerning the materials used in the preparation of the catalyst.

2.2. Materials characterization

X-ray diffraction (XRD) patterns were acquired using a MAXima_X XRD-7000 diffractometer employing Cu $K\alpha$ radiation and operating at 40 kV and 40 mA. The microscopic morphology of the catalyst was assessed by obtaining transmission electron microscopy (TEM) images (Hitachi S-5500) by high-angle annular dark field scanning TEM (HAADF-STEM, JEMARM300F). X-ray photoelectron spectroscopy (XPS) was performed using an ESCALAB 250 Xi spectrometer with an Al $K\alpha$ radiation source and the spectra were corrected based on the C 1s peak at 284.6 eV. The metal content of the catalyst was determined by inductively coupled plasma atomic emission spectrometry (ICP-AES). Co K-edge X-ray absorption spectroscopy (XAS) analyses were performed at the Beijing Synchrotron Radiation Facility 1W1B station, employing a storage ring operating at 2.5 GeV with an average current of 250 mA and a Si (111) bicrystal monochromator. Data were collected in the transmission/fluorescence mode in conjunction with an ionization chamber. All spectra were collected under ambient conditions.

2.3. Degradation experiment

All electrocatalytic reduction-oxidative degradation experiments were carried out in a single-chamber reactor with a capacity of 100 mL (Fig. S1). Electrocatalytic reduction trials were performed in a double-chamber reactor in which the chambers were separated by a Nafion membrane. The prepared working electrode, Pt foil and Ag/AgCl were used as the cathode, anode, and reference electrode, respectively. The electrode potential was corrected by RHE. The working electrode was prepared by dispersing a 10 mg quantity of the catalyst in a mixture of 2.95 mL H_2O and 0.05 mL Nafion. This dispersion was then applied to a carbon paper support with a working area of 12 cm^2 . The degradations trials were performed in a solution containing $50\text{ mmol}\cdot\text{L}^{-1}$ Na_2SO_4 and $20\text{ mg}\cdot\text{L}^{-1}$ 2,4-D, the pH of which was adjusted by adding H_2SO_4 ($0.05\text{ mol}\cdot\text{L}^{-1}$) or NaOH solutions ($0.1\text{ mol}\cdot\text{L}^{-1}$). The specific energy consumption ($E_{2,4-D}$) per 2,4-D removal was calculated using the procedure outlined in Text S2. Cycling experiments were performed by washing a used $Co_1Cu_p\text{-NC}$ cathode and reusing the material. Different voltage degradation experiments were performed by varying the applied potential (-0.3 V , -0.5 V , -0.7 V and -0.9 V (vs. RHE)). The stability experiments were conducted on a CHI660D electrochemical workstation. All data points shown in the figures herein represent the averages

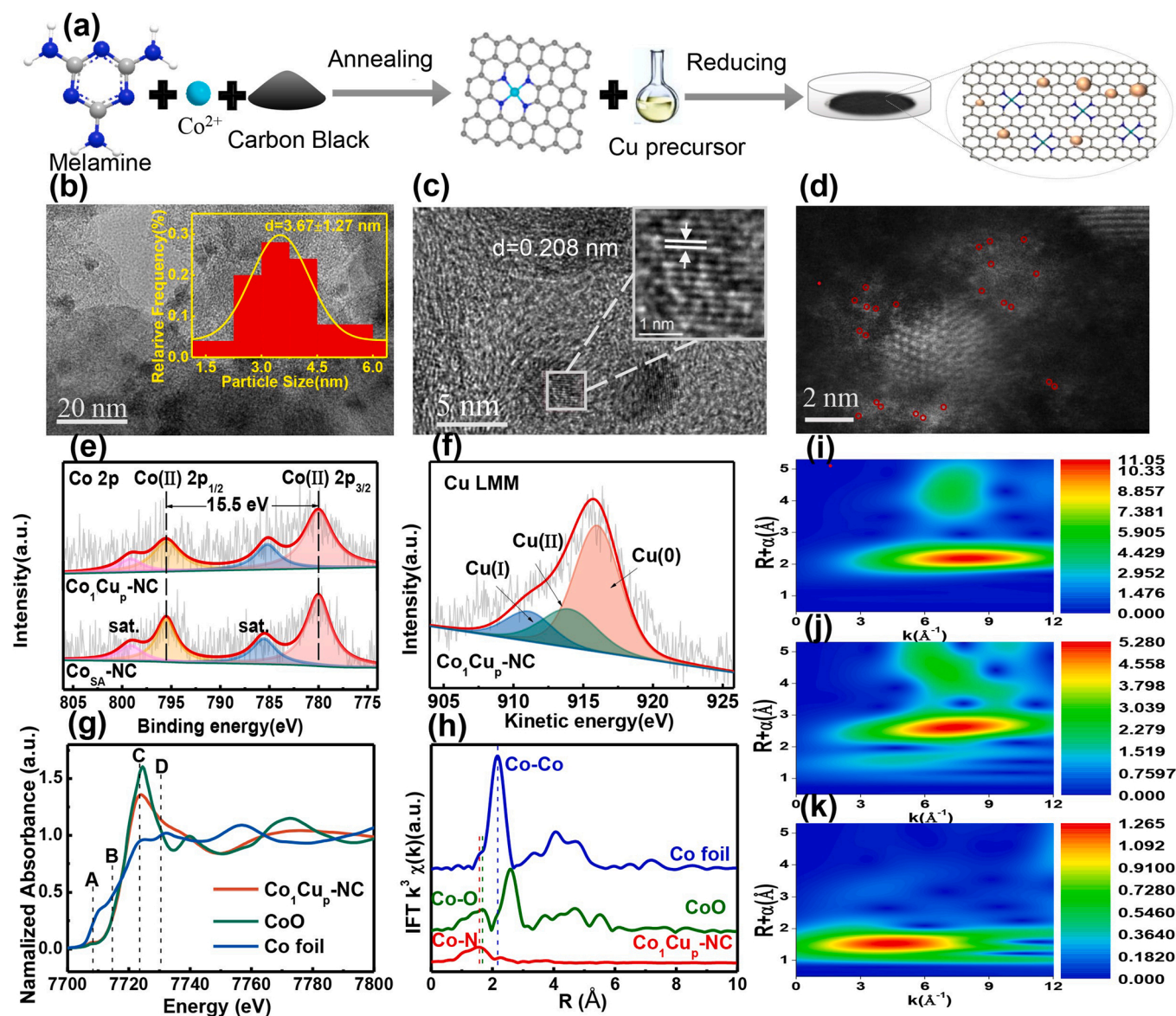


Fig. 1. (a) The fabrication procedure of the $\text{Co}_1\text{Cu}_\text{P}\text{-NC}$. (b, c) TEM images of the $\text{Co}_1\text{Cu}_\text{P}\text{-NC}$. (d) HAADF-STEM images of the $\text{Co}_1\text{Cu}_\text{P}\text{-NC}$. (e) Co 2p XPS spectra of the $\text{Co}_1\text{Cu}_\text{P}\text{-NC}$. (f) Cu LMM spectra of the $\text{Co}_1\text{Cu}_\text{P}\text{-NC}$. (g) Normalized XANES spectra at the Co K edge of $\text{Co}_1\text{Cu}_\text{P}\text{-NC}$, Co foil and CoO. (h) Co K edge k^3 -weighted FT-EXAFS spectrum of $\text{Co}_1\text{Cu}_\text{P}\text{-NC}$, Co foil and CoO. (i-k) WT-EXAFS of Co foil, CoO, and $\text{Co}_1\text{Cu}_\text{P}\text{-NC}$.

of three replicate trials and include error bars.

2.4. Analytical method

The concentration of H_2O_2 in the electrocatalytic system was determined by spectrometry using a potassium titanyl oxalate method with a U-2910 spectrophotometer (Hitachi, Japan). The concentration of 2,4-D, o-chlorophenoxyacetic acid (o-CPA), p-chlorophenoxyacetic acid (p-CPA), phenoxyacetic acid (PA), 2,4-dichlorophenol (2,4-DCP) and 2-chloro-4-hydroxyphenoxyacetic acid ($\text{C}_8\text{H}_7\text{ClO}_4$) were obtained using high performance liquid chromatography (HPLC, Shimadzu LC2030) with an Athena C18 column (5 μm particle size, 4.6 mm \times 250 mm). The mobile phase was a mixture of 0.1% acetic acid and methanol (30:70, v:v) at a flow rate of 1 $\text{mL}\cdot\text{min}^{-1}$ and the detection wavelength was 278 nm. Intermediates generated during 2,4-D degradation were analyzed using liquid chromatography-mass spectrometry (LC-MS, Agilent QTOF 6540) operating in the electrospray positive ion mode. Chloride concentrations were determined by ion chromatography (IC-300, Diane, American). Total organic carbon (TOC) was measured using

a TOC analyzer (TOC-L CSH, Shimadzu, Japan). Electron paramagnetic resonance (EPR) spectra were acquired in a single-chamber reactor without contaminants. Text S3 provides detailed information regarding the electrochemical analyses while the specific steps used to determine the cumulative $\cdot\text{OH}$ concentrations are provided in Text S4.

2.5. Theoretical calculation

The DFT calculations were performed using the Vienna ab initio Simulation Program (VASP) to calculate the predicted density of states of the active metal sites, the adsorption energy for 2,4-D and the free energy of the potential pathway for the H_2O_2 reaction [45,46]. The Gaussian 09 W and Multiwfn 3.8 software packages were used to perform DFT simulations to determine the sites of pollutant molecules that were most likely to be attacked during the degradation process [47, 48]. Text S5 provides more details concerning the theoretical calculations.

3. Results and discussion

3.1. Structural and electronic properties of $\text{Co}_1\text{Cu}_p\text{-NC}$

The synthesis process of the $\text{Co}_1\text{Cu}_p\text{-NC}$ electrode was illustrated in Fig. 1a. The TEM images in Fig. S2a-c demonstrate that the NC substrate had an irregular, wrinkled structure that would be expected to assist in exposing active sites and to promote mass transfer. The XRD pattern in Fig. S3a has only very weak peaks related to the metals, indicating that minimal amounts of Co and Cu were anchored on the NC and that these metals were well dispersed. The TEM image of the $\text{Co}_{\text{SA}}\text{-NC}$ in Fig. S2f shows that the Co clusters could not be observed even at a resolution of 5 nm, providing further evidence for the high degree of dispersion of the Co. However, the TEM images in Fig. 1b and c confirm the presence of uniformly deposited Cu nanoclusters with sizes of 2–5 nm. The lattice fringes with spacing $d = 0.208$ nm in the HR-TEM image can be attributed to the Cu (111) crystal plane of the Cu nanoclusters (Fig. 1c). Atomically-dispersed Co centers on the NC can be clearly identified in the high magnification HAADF-STEM image in Fig. 1d based on the presence of bright spots. The distance between Cu cluster and the Co- N_4 site was 0.5–1.7 nm observed from HAADF-STEM. The three-dimensional size of the optimal molecular structure for 2,4-D is $1.2625 \times 0.8208 \times 0.4018 \text{ nm}^3$ [49]. The distance between the 2,4-D on the adsorption site and $^*\text{OH}$ produced by the Co- N_4 site is about 0.5 nm, indicating that the synergistic catalytic process can be satisfied [50,51]. The Cu and Co in the $\text{Cu}_p\text{-NC}$ and $\text{Co}_{\text{SA}}\text{-NC}$ catalysts, respectively, appeared to be in the same state as those present in the $\text{Co}_1\text{Cu}_p\text{-NC}$ (Figs. S2 and S4). Raman spectroscopy also verified that metal doping increased the concentration of defects in the carbon, which would be expected to increase the performance of the catalyst (Fig. S3b).

Analyses by XPS were used to establish the surface composition and chemical states of the $\text{Co}_1\text{Cu}_p\text{-NC}$. The spectra in Fig. S5 clearly show signals related to C, O, N, Co, and Cu, indicating that Co and Cu were applied to the surface of the substrate material. The C, N and O in each catalyst produced very similar spectra and evidently had consistent valence states. The high-resolution N 1s spectrum all show five peaks (Fig. S6) that can be primarily attributed to pyridinic N (398.3 eV) and pyrrolic N (401.0 eV) coordinated by metal N (399.5 eV). After the metal Co was anchored, the pyridinic N content of the material was decreased (Table S1). This effect is attributed to the significant energy splitting between the N σ^* and π^* orbitals of the pyridinic N at the K edge and the lower N 1s orbitals. This splitting promotes d orbital hybridization with the transition metal atoms [52]. The pyridinic N atoms in these catalysts were able to act as anchors to stabilize single Co atoms [53] such that active Co- N_x sites may have been formed [48].

Satellite Co $2p_{3/2}$ and Co $2p_{1/2}$ peaks appeared at 780.0 and 795.5 eV, respectively, in the Co 2p XPS spectra (Fig. 1e) [54,55]. The Cu $2p_{3/2}$ spectrum corresponded to Cu (0) or Cu (I) (932.2 eV) and Cu (II) (934.2 eV) (Fig. S7) [56]. The binding energy overlap of the Cu 2p spin-orbit components of Cu (0) and Cu (I) makes it very difficult to separate the respective contributions and quantify the relative contributions. Determination of valence state of Cu by Auger electron spectroscopy. From the Cu Laser Microbeam Microdissection (LMM), the catalyst is mainly present as Cu (0) (916.0 eV) (Fig. 1f) [57]. The presence of Cu (I) and Cu (II) may be the result of the oxidation of Cu (0) on the surface. ICP-AES analyses indicated that the Co and Cu concentrations in the $\text{Co}_1\text{Cu}_p\text{-NC}$ were 1.39 and 2.02 wt%, respectively (Table S2), confirming that both metals were successfully incorporated into the $\text{Co}_1\text{Cu}_p\text{-NC}$. In addition, the concentrations and binding energy positions of the Co and Cu were unchanged after this deposition, indicating that Co-Cu bonds were not formed and that the metals were deposited independent of one another. There were only minimal variations in the Co peak position and concentration (0.2 at% after acid etching) before and after acid etching and a characteristic Cu peak was not observed after etching (Fig. S8). From these results, it is evident that the single atom Co structure was stable under reducing conditions.

The chemical state, coordination environment and local electronic structure of Co in the $\text{Co}_1\text{Cu}_p\text{-NC}$ were studied by X-ray absorption fine structure (XAFS) spectroscopy, using CoO and Co foil standards for comparison. In Fig. 1g, the $\text{Co}_1\text{Cu}_p\text{-NC}$ spectrum is comparable to that of CoO at the Co K edge at half of the maximum strength of the edge, indicating that the valence state of the Co in the specimen was essentially the same as that of CoO. This result means that the Co was primarily in the Co (II) unsaturated state. The front edge peak at 7709.0 eV was attributed to the $1s \rightarrow 3d$ transition of Co, suggesting that the D_{4h} center of symmetry at each Co site was distorted. Compared with CoPc, the Co K-edge XANES data obtained from the $\text{Co}_1\text{Cu}_p\text{-NC}$ lacked a front edge feature at approximately 7715 eV resulting from the $1s$ to $4p$ transition. This result can be attributed to the difference in the geometric structure associated with metal-N coordination in the $\text{Co}_1\text{Cu}_p\text{-NC}$ compared with that in CoPc. That is, the Co atoms were coordinated with pyridinic N in the $\text{Co}_1\text{Cu}_p\text{-NC}$, while the Co in CoPc was coordinated with pyrrolic N [58].

More detailed information concerning the atomic Co in the specimens was obtained by Fourier transform (FT) extended X-ray absorption fine structure (EXAFS) spectroscopy. As shown in Fig. 1h, the Co K-edge FT EXAFS spectrum of $\text{Co}_1\text{Cu}_p\text{-NC}$ exhibited a nearest-neighbor signal at 1.6 \AA corresponding to a Co-N-C layer similar that occurring in tetrahedral coordination (Co- N_4) [59]. The absence of the Co-Co coordination peak at 2.2 \AA and the absence of the Co-Cu coordination peak at 2.6 \AA in the Co K-edge FT-EXAFS spectrum of $\text{Co}_1\text{Cu}_p\text{-NC}$ excluded the formation of the Co nanoclusters and Co-Cu coordination [60]. An EXAFS wavelet transform (WT) analysis can easily distinguish back-scattered atoms that may overlap in R space and can also provide the radial distance and k spatial resolution [61]. It can be seen from Fig. 1i-k that there was only one maximum intensity in the WT diagram of the $\text{Co}_1\text{Cu}_p\text{-NC}$, at approximately 5.5 \AA^{-1} , ascribed to Co-N bonds. It indicated that the catalyst samples did not contain metal bonds related to Co-Co (6.2 \AA^{-1}) and Co-Cu (6.6 \AA^{-1}) [62]. The WT-EXAFS results also confirmed that the Co in the $\text{Co}_1\text{Cu}_p\text{-NC}$ was present in the form of single atoms. A quantitative least square fitting of the EXAFS data was performed (Fig. S9) to analyze the coordination configuration of the Co atoms in the $\text{Co}_1\text{Cu}_p\text{-NC}$ and the resulting coordination parameters are summarized in Table S3. On this basis, the Co-N bond coordination number in the $\text{Co}_1\text{Cu}_p\text{-NC}$ was determined to be approximately 4. In summary, the X-ray absorption characteristics of the $\text{Co}_1\text{Cu}_p\text{-NC}$ catalyst confirmed the successful preparation of Co- N_4 species.

3.2. Degradation of 2,4-D using $\text{Co}_1\text{Cu}_p\text{-NC}$ cathodes

Varying the composition of the catalytic cathode was found to affect the degradation of 2,4-D. In the $\text{Co}_1\text{Cu}_p\text{-NC}$ cathodic electrocatalytic system, the 2,4-D was almost completely degraded after 60 min, showing excellent degradation (Fig. 2a). In contrast, the 2,4-D removal efficiencies observed using the NC, $\text{Cu}_p\text{-NC}$ and $\text{Co}_{\text{SA}}\text{-NC}$ cathodes at 60 min were 54.9%, 90.9% and 74.8%, respectively. To exclude the loss of 2,4-D by electrosorption (EA) and anodic oxidation (AO) processes, comparative experiments were carried out. In these trials, EA was induced by applying a voltage of -0.1 V with a N_2 purge while AO was performed in a double-chamber reactor separated by a Nafion proton exchange membrane. Fig. S10 shows that only 5.1% and 13.3% of the 2,4-D were removed by EA and AO, respectively, indicating that the catalytic cathode system made the primary contribution to the degradation of 2,4-D in this system. The efficient degradation of 2,4-D was evidently possible using the $\text{Co}_1\text{Cu}_p\text{-NC}$ electrode.

In additional trials, various kinetics data were obtained by carrying out the electrolysis of 2,4-D using different cathodes. As shown in Fig. S11a, the 2,4-D degradation reaction on these electrodes followed first-order kinetics. The kinetics constants (k) for the NC, $\text{Cu}_p\text{-NC}$, $\text{Co}_{\text{SA}}\text{-NC}$ and $\text{Co}_1\text{Cu}_p\text{-NC}$ were calculated to be 0.01157, 0.03968, 0.02121 and 0.05745 min^{-1} , respectively (Fig. S11b). To obtain an improved understanding of the kinetics of the conversion reaction at the active

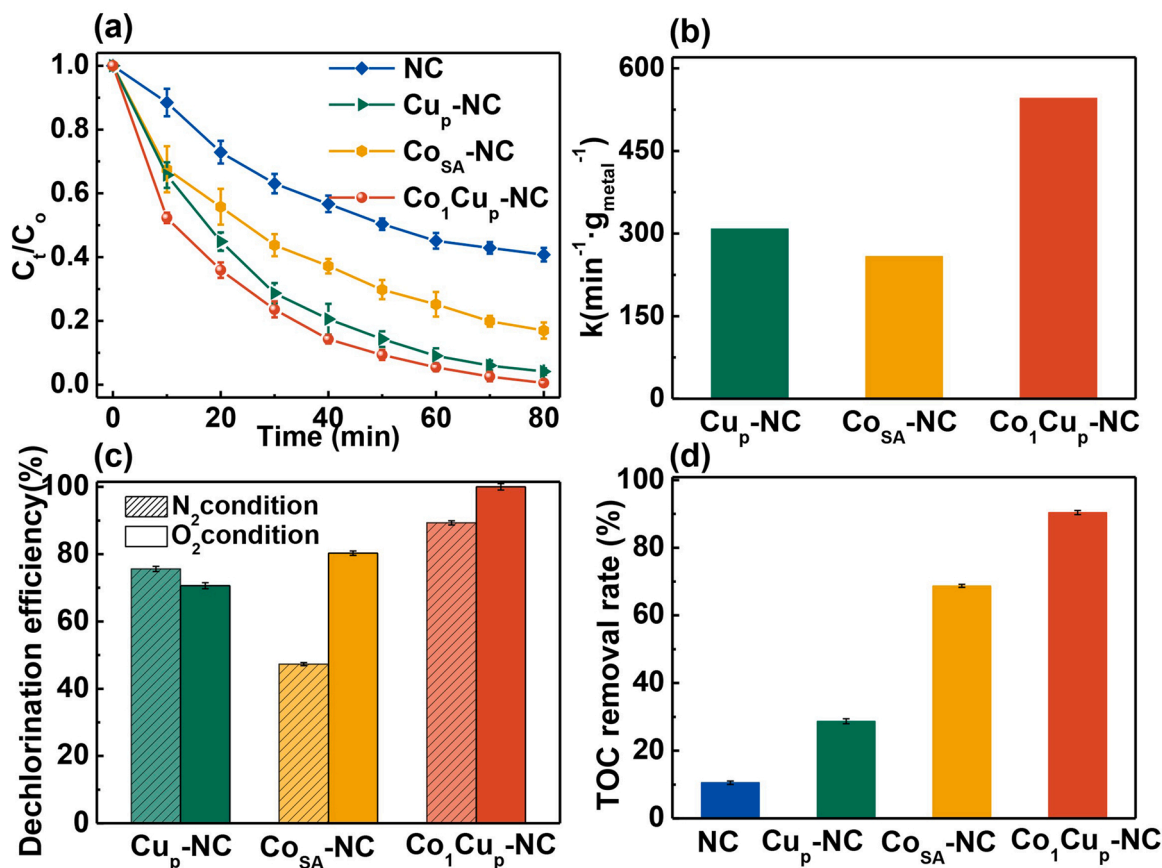


Fig. 2. (a) 2,4-D degradation on different electrodes. (b) Mass activities in the kinetic rate (k_{metal}) of 2,4-D degradation. (c) Dechlorination efficiency on different electrodes. (d) TOC removal efficiency on different electrodes. Reaction condition: [2,4-D] = 20 mg·L⁻¹, pH = 5, and potential = -0.5 V.

metal sites, the k values were subsequently normalized relative to the unit mass of metal in the catalyst (k_{metal}). As shown in Fig. 2b, the k_{metal} for 2,4-D decomposition on the Co₁Cu_p-NC was 546.4 min⁻¹·g_{metal}⁻¹ and so was increased relative to the values for the Cu_p-NC (309.1 min⁻¹·g_{metal}⁻¹) and Co_{SA}-NC (258.9 min⁻¹·g_{metal}⁻¹) by factors of 1.8 and 2.1, respectively. The turnover number (TON) of 2,4-D degradation is calculated. The TON values of Co₁Cu_p-NC, Co_{SA}-NC, and Cu_p-NC are 3.18, 2.72, and 3.46, respectively. These results indicate that the synergy of Cu cluster and the Co-N₄ site promotes 2,4-D degradation. The Co₁Cu_p-NC in the present work also showed excellent organic pollutant degradation performance when compared with previously reported electrocatalysts (Table S4).

The 2,4-D dechlorination efficiency during electrocatalytic reduction-oxidation was calculated by monitoring the Cl⁻ ion concentration and the results are presented in Fig. 2c [63]. Theoretically, a Cl⁻ concentration of 6.4 mg·L⁻¹ should be generated from a 20 mg·L⁻¹ solution of 2,4-D and reactions under O₂ for 80 min using the Cu_p-NC, Co_{SA}-NC and Co₁Cu_p-NC catalytic cathodes produced concentrations of 5.1, 4.5 and 6.0 mg·L⁻¹, respectively. The dechlorination efficiency obtained from the Co₁Cu_p-NC cathode was therefore close to 100% while the Cu_p-NC and Co_{SA}-NC cathodes exhibited efficiencies of 80.3% and 70.6%, respectively. The concentrations of Cl⁻ released after 80 min from reactions under N₂ are shown in Fig. 2c and indicate that the dechlorination efficiencies of the Cu_p-NC, Co_{SA}-NC and Co₁Cu_p-NC cathodes in this case were 75.6%, 47.3% and 89.3%, respectively. In reactions involving the Co_{SA}-NC cathode, it is apparent that indirect oxidation played a part in determining the dechlorination efficiency while the 80.3% dechlorination efficiency of the Cu_p-NC cathode was primarily a result of direct reduction. The dechlorination efficiency of Co₁Cu_p-NC degradation of 2,4-D was 100%, which contained 89.3% of reductive dechlorination and 10.7% of oxidative dechlorination. The

complete dechlorination of 2,4-D using the Co₁Cu_p-NC was achieved as a result of a synergistic combination of reductive dechlorination and oxidative dechlorination. This synergistic effect is mainly due to the electron donor Cu cluster site, which has a low standard redox potential to reduce 2,4-D by direct electron transfer to produce chlorine-free intermediates, and the precisely regulated Co-N₄ site, which is capable of indirect oxidative dechlorination via ·OH generated by O₂ reduction reactions.

Variations in the TOC values of the reaction solutions were also studied. The proportional TOC decreases after 2 h of 2,4-D electrolysis using NC, Cu_p-NC, Co_{SA}-NC and Co₁Cu_p-NC cathodes were 10.6%, 28.7%, 68.7% and 93.4%, respectively (Fig. 2d). The TOC decrease obtained from the Co_{SA}-NC was comparable to the extent of dechlorination observed when using this material (70.6%), further indicating that indirect oxidation played a dominant role in the reaction over the Co_{SA}-NC cathode. The 93.4% mineralization efficiency and 100% dechlorination efficiency of the Co₁Cu_p-NC catalytic cathode established that 2,4-D was effectively decomposed into non-toxic low molecular weight molecules. The efficient mineralization exhibited by the Co₁Cu_p-NC is primarily attributed to the ability of the active Co atom sites to promote oxidation during the electrocatalytic reduction-oxidation process. The superior performance of the Co₁Cu_p-NC could also result from enhanced electron transport. Prior studies have demonstrated that both the generation of ROS and the electron transfer associated with electrode materials play important roles in the degradation of organic pollutants [8,64]. For this reason, the Co₁Cu_p-NC cathode exhibited excellent electron transfer and ROS generation characteristics, meaning that is improved 2,4-D degradation efficiency, a higher kinetics rate constant and greater TOC removal compared with the other electrodes. Therefore, this cathode was selected for use in subsequent experiments exploring the key active sites and degradation mechanism.

The applied voltage evidently affected the generation of ROS during the degradation of 2,4-D and this effect was thus studied in more detail. As shown in Fig. S12a, the degradation efficiency increased as the voltage was increased from -0.3 to -0.7 V (vs. RHE). It was due to higher voltages promoted the catalytic production of active substances by the $\text{Co}_1\text{Cu}_p\text{-NC}$. In contrast, a voltage of -0.9 V (vs. RHE) lowered the efficiency of the system because the hydrogen evolution reaction was promoted on the electrode surface [65]. The hydrogen evolution overpotential was -0.81 V (vs. RHE), which were between -0.9 and -0.7 V (vs. RHE) (Fig. 3a). In addition, the 2,4-D degradation rates over this material could be explained using a pseudo-first-order kinetics equation (Fig. S12b) and the reaction rate constant for 2,4-D degradation at -0.5 V (vs. RHE) was higher than that at -0.7 V (vs. RHE) (Fig. 3b) while the time required to completely remove the 2,4-D was unchanged.

The energy consumption ($E_{2,4\text{-D}}$) per unit of removed 2,4-D is a key parameter related to evaluating the energy consumption of the electrochemical process [66] and the method used to calculate this parameter in the present work is provided in Text S2. As shown in Fig. 3c, the $E_{2,4\text{-D}}$ value gradually increased as the applied voltage was increased from -0.3 to -0.9 V (vs. RHE). Above -0.5 V (vs. RHE), $E_{2,4\text{-D}}$ exhibited an especially sharp increase, indicating that this was the most suitable voltage value ($0.033 \text{ kWh}\cdot\text{g}^{-1}$). Therefore, an applied voltage of -0.5 V (vs. RHE) was selected for subsequent 2,4-D degradation experiments.

Electrolytes having different pH values were used to explore the stability of the $\text{Co}_1\text{Cu}_p\text{-NC}$ electrocatalytic system. From Fig. 3d, it is apparent that the degradation efficiency changed only minimally, from 0.05212 to 0.05945 min^{-1} , as the pH was varied. The presence of H^+

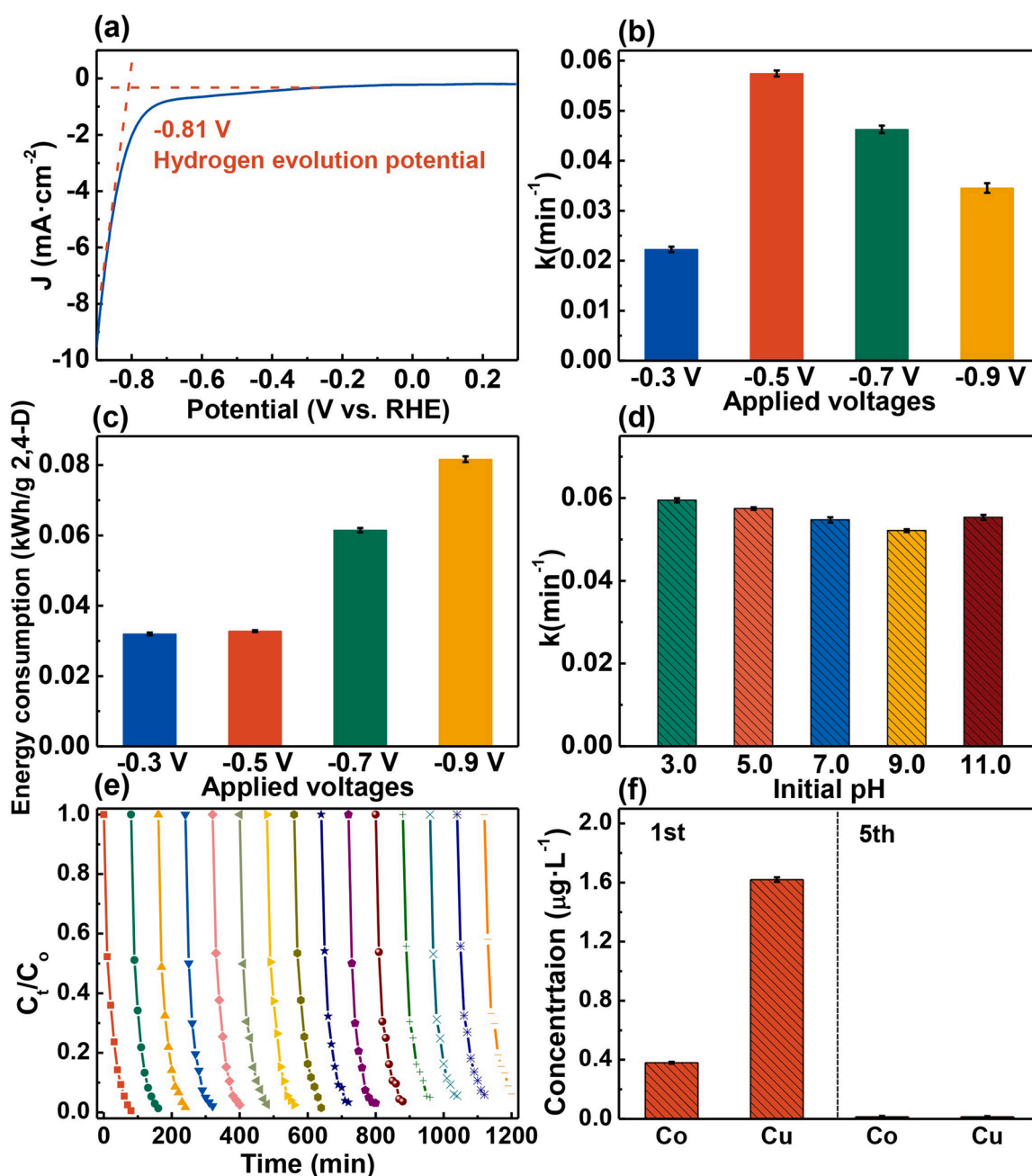


Fig. 3. (a) LSV tests on $\text{Co}_1\text{Cu}_p\text{-NC}$ catalyst. (b) Effects of applied voltage on $\text{Co}_1\text{Cu}_p\text{-NC}$ electrode on 2,4-D degradation. (c) Energy consumption under different applied voltages. (d) Effects of initial pH on the 2,4-D degradation. (e) Reusability tests. (f) The leaching properties of metal ions. Reaction condition: $[2,4\text{-D}] = 20 \text{ mg}\cdot\text{L}^{-1}$ and pH = 5.

ions associated with acidic conditions would be expected to promote the reaction while alkaline conditions would enhance the ORR. Thus, the $\text{Co}_1\text{Cu}_p\text{-NC}$ electrocatalytic system was able to effectively remove 2,4-D at different pH values.

The same $\text{Co}_1\text{Cu}_p\text{-NC}$ specimen was also found to be capable of removing 2,4-D continuously over fifteen reuses. The removal ratio of 2,4-D showed no significant change during fifteen-cycles operations, suggesting the excellent reusability of $\text{Co}_1\text{Cu}_p\text{-NC}$ (Fig. 3e). Analyses by ICP-MS (Fig. 3f) showed minimal leaching of Cu and Co ions into the reaction solution, further verifying the stability and safety of the $\text{Co}_1\text{Cu}_p\text{-NC}$ electrode when applied to pollutant removal. In addition, the XRD pattern of the used electrode showed no significant difference with the unused material in Fig. S12c. It indicated that the $\text{Co}_1\text{Cu}_p\text{-NC}$ electrode had excellent stability. The current stability of time-current curve detection also showed the excellent long-term performance of $\text{Co}_1\text{Cu}_p\text{-NC}$ cathode (Fig. S12d).

3.3. Identification and active species in the $\text{Co}_1\text{Cu}_p\text{-NC}$ system

Active species scavenging experiments were performed to identify specific ROS such as $\cdot\text{OH}$, $\cdot\text{O}_2$ and $^1\text{O}_2$ in the reaction solution. As shown in Fig. 4a, the removal of 2,4-D was inhibited as the tert-butyl alcohol (TBA) concentration was increased [67]. Specifically, increasing the concentration of TBA to $400\text{ mmol}\cdot\text{L}^{-1}$ lowered the degradation efficiency from 100% to 59.6% while an additional increase to $500\text{ mmol}\cdot\text{L}^{-1}$ decreased the efficiency only slightly more (to 57.4%). These data suggest that all the $\cdot\text{OH}$ generated in the system had been removed at a concentration of $400\text{ mmol}\cdot\text{L}^{-1}$. However, the degradation of 2,4-D was not completely inhibited by the presence of TBA and so other radicals and/or non-radicals were likely involved in the system.

The addition of p-benzoquinone (p-BQ) did not inhibit the degradation of 2,4-D, indicating that the contribution of $\cdot\text{O}_2$ was negligible (Fig. S13a). The addition of furfuryl alcohol (FFA) as a scavenger of $^1\text{O}_2$ had little effect such that the degradation efficiency was decreased by only 8.7% (Fig. S13a) [68].

EPR spectroscopy was used to further assess the participation of $\cdot\text{OH}$, $\cdot\text{O}_2$ and $^1\text{O}_2$ in the decomposition process [69]. The intensity of the characteristic DMPO- $\cdot\text{OH}$ peak was found to increase over time, confirming the continuous generation of $\cdot\text{OH}$ (Fig. 4b). The DMPO- $\cdot\text{O}_2$ and TEMPO- $^1\text{O}_2$ signals were almost absent and so $\cdot\text{O}_2$ and $^1\text{O}_2$ were evidently not active in the system. BA, NBT and FFA were selected as chemical probes to quantify $\cdot\text{OH}$, $\cdot\text{O}_2$ and $^1\text{O}_2$ [70]. The concentration of BA was found to decrease with reaction time, indicating that $\cdot\text{OH}$ radicals were generated in the $\text{Co}_1\text{Cu}_p\text{-NC}$ electrocatalytic system (Fig. S14a). The NBT concentration remained unchanged throughout the reaction, meaning that $\cdot\text{O}_2$ was not produced (Fig. S14b) [67]. Similarly, $^1\text{O}_2$ was not a primary reactant (Fig. S14c). The $[\cdot\text{OH}]$, $[\cdot\text{O}_2]$ and $[^1\text{O}_2]$ values in the reaction solution were calculated (Fig. 4c) and provided further evidence of $\cdot\text{OH}$ generation. Based on the above results, $\cdot\text{OH}$ evidently played the dominant role in 2,4-D degradation. However, when a high concentration of TBA ($500\text{ mmol}\cdot\text{L}^{-1}$) was added, 47.4% of the 2,4-D was still removed and so it appears that other 2,4-D degradation processes occurred in addition to oxidation by $\cdot\text{OH}$. Trials involving the electroreduction of 2,4-D were carried out (Figs. 3f) and 83.7% removal was obtained within 60 min. These results showed that electroreductive dechlorination was possible using the $\text{Co}_1\text{Cu}_p\text{-NC}$ system.

The electroreduction performance of the present system was also assessed using LSV. As shown in Fig. S15, the reduction current densities generated by all the catalysts increased following the addition of 2,4-D, suggesting that this compound was reduced on these materials. At

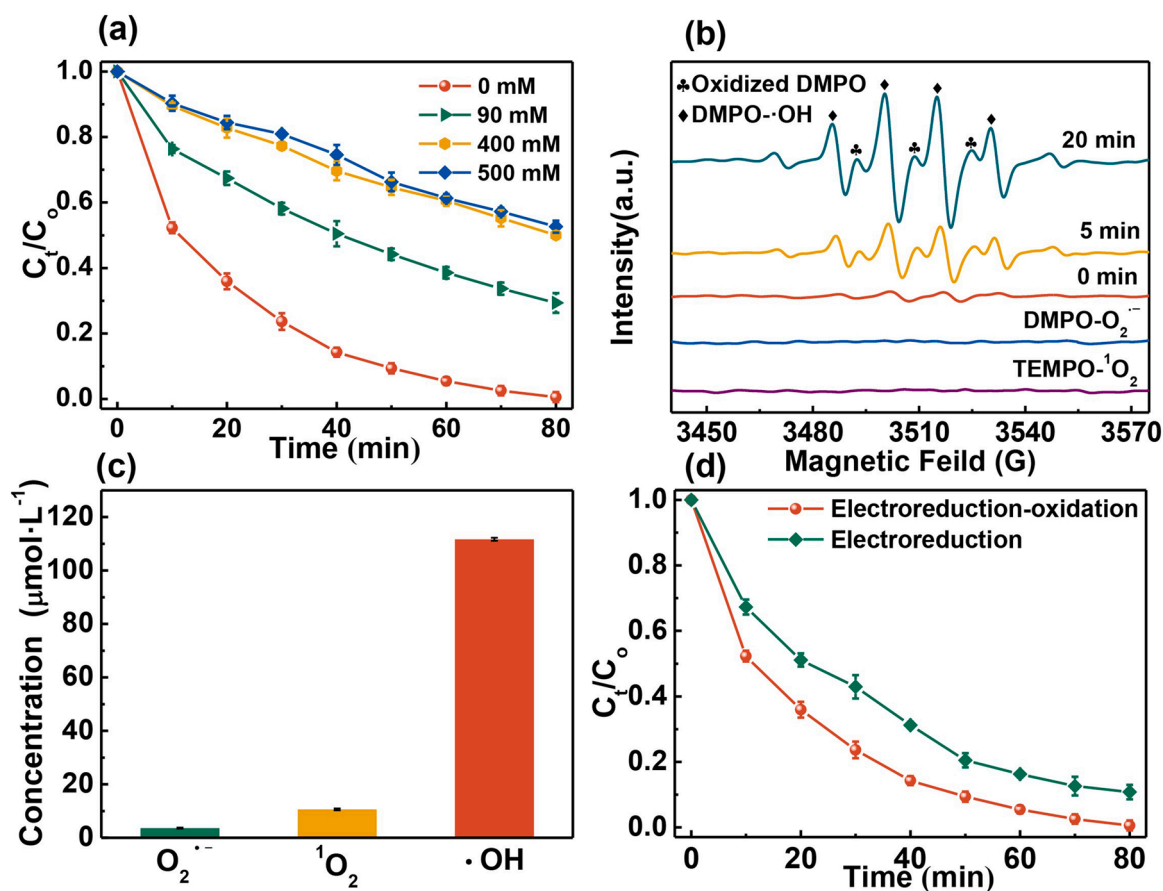


Fig. 4. (a) Effects of TBA on the 2,4-D degradation. (b) Spin-trapping EPR spectra. (c) The quantitative concentration of reactive oxygen species. (d) Degradation of 2,4-D by different electrochemical processes. Reaction condition: $[\text{2,4-D}] = 20\text{ mg}\cdot\text{L}^{-1}$, pH = 5, and potential = -0.5 V .

−0.5 V (vs. RHE), the current density associated with 2,4-D reduction on the $\text{Co}_1\text{Cu}_p\text{-NC}$ was $1.96 \text{ mA}\cdot\text{cm}^{-2}$, which exceeded the value for the other specimens. The $\text{Co}_1\text{Cu}_p\text{-NC}$ catalyst also showed the lowest resistance. Thus, the synergistic effect of the Co and Cu sites seems to have improved the interfacial charge separation efficiency, facilitated interfacial reactions, and provided superior electron transfer characteristics (Fig. 5b and Table S5). The electron transfer capacities decreased in the order of $\text{Co}_1\text{Cu}_p\text{-NC} > \text{Cu}_p\text{-NC} > \text{Co}_{\text{SA}}\text{-NC} > \text{NC}$, indicating that Cu promoted 2,4-D reduction to a greater extent than Co.

In addition, 2,4-D electroreduction dechlorination trials were carried out. From the data in Fig. 5a it is apparent that the $\text{Co}_1\text{Cu}_p\text{-NC}$ catalytic cathode exhibited the highest electrochemical reduction capacity, with an efficiency of 85.8% after 60 min. This was followed by the $\text{Cu}_p\text{-NC}$ (75.6%), $\text{Co}_{\text{SA}}\text{-NC}$ (61.9%) and NC (46.7%). The electroreduction k_{metal}

value for the $\text{Co}_1\text{Cu}_p\text{-NC}$ electrode was $269.3 \text{ min}^{-1}\cdot\text{g}_{\text{metal}}^{-1}$. This value was 1.6 times and 1.4 times greater than those for the $\text{Cu}_p\text{-NC}$ ($191.2 \text{ min}^{-1}\cdot\text{g}_{\text{metal}}^{-1}$) and $\text{Co}_{\text{SA}}\text{-NC}$ ($160.5 \text{ min}^{-1}\cdot\text{g}_{\text{metal}}^{-1}$), respectively (Fig. S16b). These findings suggest that the synergistic effect resulting from a combination of Co and Cu promoted the electroreduction of the 2,4-D. In the $\text{Co}_1\text{Cu}_p\text{-NC}$ electrocatalytic degradation of 2,4-D systems, the active species for dechlorination may be hydrogen atoms, hydrated electrons, and hydroxyl radicals. The dechlorination efficiency of hydroxyl radical oxidation was 10.3%. The efficiency of dechlorination by reduction of hydrogen atoms and hydrated electrons was 89.7%. The presence of weak DMPO-H^* reflected the generation of a small amount of H^* in the catalytic system (Fig. S16c). Therefore, direct electron transfer dechlorination of hydrated electrons was the main dechlorination species [71,72].

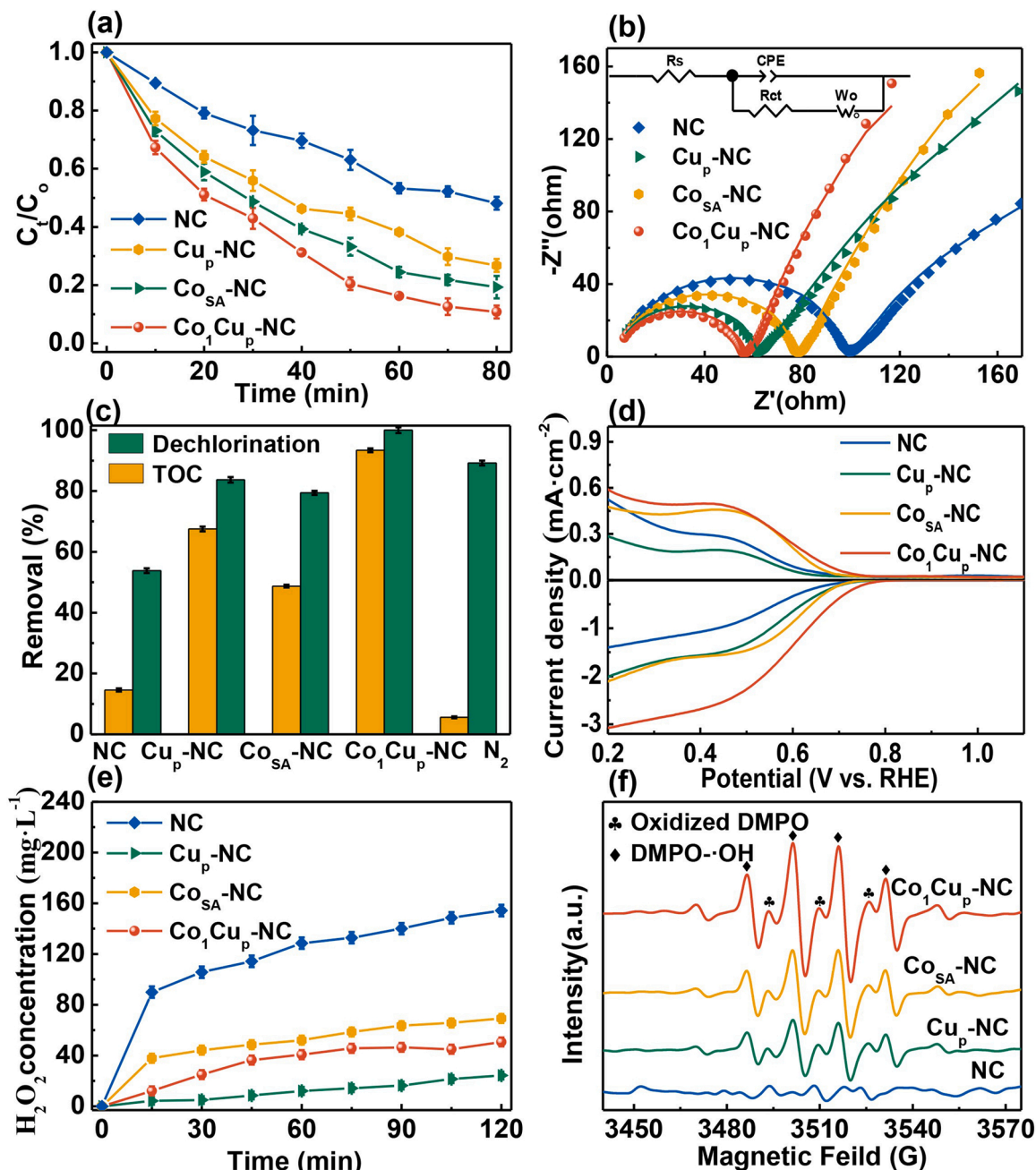
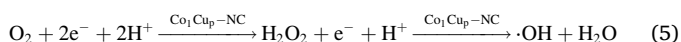
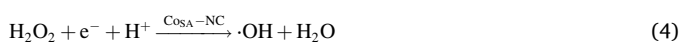


Fig. 5. (a) 2,4-D degradation on different electrodes by electrochemical reduction. (b) EIS data of the different catalysts. (c) Dechlorination effect and TOC removal of 2,4-D with different electrodes after 2 h. (d) RRDE curves of the different catalysts in an O_2 saturated electrolyte at a rotation speed of 1600 rpm. (e) H_2O_2 production on different electrodes. (f) EPR spectra in different electrodes. Reaction condition: $[\text{2,4-D}] = 20 \text{ mg}\cdot\text{L}^{-1}$, $\text{pH} = 5$, and potential = -0.5 V .

The production of $\cdot\text{OH}$ in the reaction system was examined by assessing the oxygen reduction performance using CV and rotating ring disk electrode trials to evaluate the ORR. Trials in which sufficient oxygen was provided showed that the $\text{Co}_1\text{Cu}_p\text{-NC}$ generated the largest reduction peak (Fig. S17a). The addition of Cu to the catalyst shifted the onset potential positively by 0.02 V and so increased the ORR activity. However, a drop in the ring current indicated a decrease in selectivity for the $2e^-$ ORR (Fig. 5d). By accurately regulating the coordination environment of Co atoms, the onset potential was shifted positively by 0.03 V and the ring current was increased. In addition, the incorporation of both Co and Cu on the NC shifted the onset potential positively by 0.08 V and significantly increased the ORR activity. The $\text{Co}_1\text{Cu}_p\text{-NC}$ electrocatalytic degradation system exhibited the higher the oxygen reduction reaction (ORR) activity which favor the generation of H_2O_2 and the faster production of $\cdot\text{OH}$ which benefit the degradation of 2,4-D [73]. At the same time, the increase in the ring current significantly increased selectivity for the $2e^-$ ORR. The H_2O_2 selectivity of catalysts were measured by RRDE. The selectivity of the $\text{Cu}_p\text{-NC}$, CoSA-NC and $\text{Co}_1\text{Cu}_p\text{-NC}$ catalysts for H_2O_2 production was 52%, 75% and 90%, respectively (Fig. S17b). It indicated that the ORR process preferentially underwent two electron transfers to produce H_2O_2 , which facilitates the mineralization of contaminants.

The H_2O_2 production of the NC catalytic cathode reached $115.7 \text{ mg}\cdot\text{L}^{-1}$ after 120 min (based on the reaction in Eq. 1) (Fig. 5e), while the yields of H_2O_2 from the $\text{Cu}_p\text{-NC}$, CoSA-NC and $\text{Co}_1\text{Cu}_p\text{-NC}$ were relatively low at 24.3, 69.3 and $50.7 \text{ mg}\cdot\text{L}^{-1}$, respectively. The $\text{Cu}_p\text{-NC}$ catalyzed the cathodic oxygen reduction process involving the transfer of $4e^-$ to produce a very small amount of H_2O_2 (Eq. 2). The small amounts of H_2O_2 observed in trials using the CoSA-NC and $\text{Co}_1\text{Cu}_p\text{-NC}$ possibly resulted from the decomposition of H_2O_2 by the single Co atoms (Eq. 3). Although the $\text{Co}_1\text{Cu}_p\text{-NC}$ exhibited higher H_2O_2 selectivity and activity than the CoSA-NC , the cumulative concentration of H_2O_2 obtained from the former was lower than that from the latter (Eq. 4). This result can possibly be attributed to the effect of Cu clusters around the Co single atoms in the $\text{Co}_1\text{Cu}_p\text{-NC}$, which promoted the decomposition of H_2O_2 . That is, H_2O_2 produced by the $2e^-$ ORR was subsequently transitioned to hydroxyl radicals via a $1e^-$ process (Eq. 5). In the case of the $\text{Co}_1\text{Cu}_p\text{-NC}$ catalytic system, the electrogenerated H_2O_2 produced around the Co atoms functioned as a reaction intermediate and was decomposed *in situ* by the Co to generate $\cdot\text{OH}$.



The catalytic decomposition of H_2O_2 was also assessed. As shown in Fig. S18, the decomposition of H_2O_2 decreased in the order of $\text{Co}_1\text{Cu}_p\text{-NC} > \text{CoSA-NC} > \text{Cu}_p\text{-NC}$. This result indicated that Co atoms could activate H_2O_2 to produce $\cdot\text{OH}$, consistent with the RRDE and H_2O_2 yield results. The $\text{Co}_1\text{Cu}_p\text{-NC}$ showed the greatest capacity for H_2O_2 activation because the atomically distributed Co effectively captured O_2 to produce and activate H_2O_2 based on precise regulation of the coordination environment. These factors improved the selectivity for and activity of the $2e^-$ ORR as well as the ability of the catalyst to activate H_2O_2 by adjusting the microelectronic environment via the surrounding Cu clusters. In addition, DMPO- $\cdot\text{OH}$ spin-trapping EPR spectra were acquired (Fig. 5f) and the NC catalyst did not produce an $\cdot\text{OH}$ peak. The $\text{Co}_1\text{Cu}_p\text{-NC}$ generated a stronger DMPO- $\cdot\text{OH}$ peak than both the $\text{Cu}_p\text{-NC}$ and CoSA-NC , which can be attributed to the formation of a higher

concentration of $\cdot\text{OH}$ by the former material. Together, these data confirm that the $\text{Co}_1\text{Cu}_p\text{-NC}$ electrode was not only the most efficient electrocatalyst for the $2e^-$ ORR but also the best catalyst in terms of activating H_2O_2 to produce hydroxyl radicals through a $1e^-$ mechanism.

3.4. Theoretical calculations regarding 2,4-D conversion

The source of the electrocatalytic reduction-oxidation activity shown by the $\text{Co}_1\text{Cu}_p\text{-NC}$ was investigated by performing DFT calculations to better understand the coupling of Cu clusters and Co single atom active sites. Based on the experimental results in Fig. 6a-c, three optimized structural models were established, comprising a Co-N_4 structure, Cu nanoclusters and a combination of Co-N_4 sites and Cu nanoclusters. Fig. S22 shows the site evolution of 2,4-D adsorption before and after the structural relaxation of the DFT process on the three catalysts surfaces. As shown in Fig. 6d and Table S8, the adsorption energies of 2,4-D on the active centers of CoSA-NC , $\text{Cu}_p\text{-NC}$ and $\text{Co}_1\text{Cu}_p\text{-NC}$ catalysts were -0.48 , -0.92 , and -1.13 eV , respectively, indicating that the Co and Cu active sites were able to interact with the carboxyl group in the 2,4-D molecule to form chemical bonds. 2,4-D could be adsorbed and subsequently participate in electrochemical reactions. A strong interaction was found between the Cu sites and the 2,4-D, meaning that the Cu nanoclusters could serve as binding sites. $\text{Co}_1\text{Cu}_p\text{-NC}$ has the largest 2,4-D adsorption energy, indicating that the introduction of the Co-N_4 bond into the coupling site can promote the adsorption of 2,4-D by the Cu active site. The predicted density of states of Cu in the $\text{Co}_1\text{Cu}_p\text{-NC}$ and $\text{Cu}_p\text{-NC}$ were also calculated. It is well known that the position of the d-band center relative to the Fermi level indicates of the strength of the metal-adsorbent interaction. Specifically, higher electron density near the Fermi level allows the molecules to be adsorbed more easily [74]. The calculations indicated that the central d-band energy level of Cu nanoclusters could be increased by introducing Co-N_4 bonds to the coupling sites to enhance Cu-H interactions (Fig. 6e). In addition, the active Cu centers exhibited obvious zero-valent metal characteristics. The coupling of Co-N_4 sites with Cu nanoclusters would be expected to provide more efficient electron transfer and good electrical conductivity such that electrons would migrate rapidly from the $\text{Co}_1\text{Cu}_p\text{-NC}$ to 2,4-D molecules. Thus, the direct electron transfer reductive dechlorination activity of the $\text{Co}_1\text{Cu}_p\text{-NC}$ electrode was further improved by using Cu metal to provide active centers.

The experimental results showed that $\cdot\text{OH}$ radicals were the main ROS generated following oxygen reduction at the $\text{Co}_1\text{Cu}_p\text{-NC}$ electrode. The desorption of $\cdot\text{H}_2\text{O}_2$ generated via the $2e^-$ ORR from the $\text{Co}_1\text{Cu}_p\text{-NC}$ surface (as opposed to the generation of $\cdot\text{OH}$ via the $1e^-$ pathway) was examined by calculating the free energy change associated with the potential pathway for the $\cdot\text{H}_2\text{O}_2$ reaction. The ΔG value for $\cdot\text{OH}$ formation from $\cdot\text{H}_2\text{O}_2$ on a Co site was found to be much lower than the value for the desorption of H_2O_2 , indicating that the former pathway would be more thermodynamically favorable (Fig. 6f) ($U = 0 \text{ V}$). According to Figs. 6g and 6h, the formation of $\cdot\text{OH}$ groups at the equilibrium potential ($U = 0.7 \text{ V}$) is heat-absorbing and this step is the reaction-determining step for $\cdot\text{H}_2\text{O}_2$ reduction. The reaction of $\text{Co}_1\text{Cu}_p\text{-NC}$ (0.03 eV) energy barrier is lower than that of CoSA-NC (0.08 eV), indicating that $\text{Co}_1\text{Cu}_p\text{-NC}$ is more active for $\cdot\text{H}_2\text{O}_2$ reduction. The limiting potential was determined to be 0.62 V in the CoSA-NC , while the value was 0.67 V for $\text{Co}_1\text{Cu}_p\text{-NC}$ (Figs. 6g and 6h). The higher limiting potential in $\text{Co}_1\text{Cu}_p\text{-NC}$ system more attractive as an $\cdot\text{H}_2\text{O}_2$ reduction candidate than the CoSA-NC . In addition, the coupling structures of Co-N_4 sites combined with Cu nanoclusters were determined to be smaller than those of pure Co-N_4 sites, indicating that the former structures would enhance the activation and subsequent desorption of H_2O_2 to generate $\cdot\text{OH}$. These phenomena can possibly be ascribed to electronic coupling between the single Co atoms and Cu nanoclusters. This coupling increased the strength of 2,4-D adsorption and promoted the formation of $\cdot\text{OH}$.

Chen et al. reported that the thermodynamic overpotential of

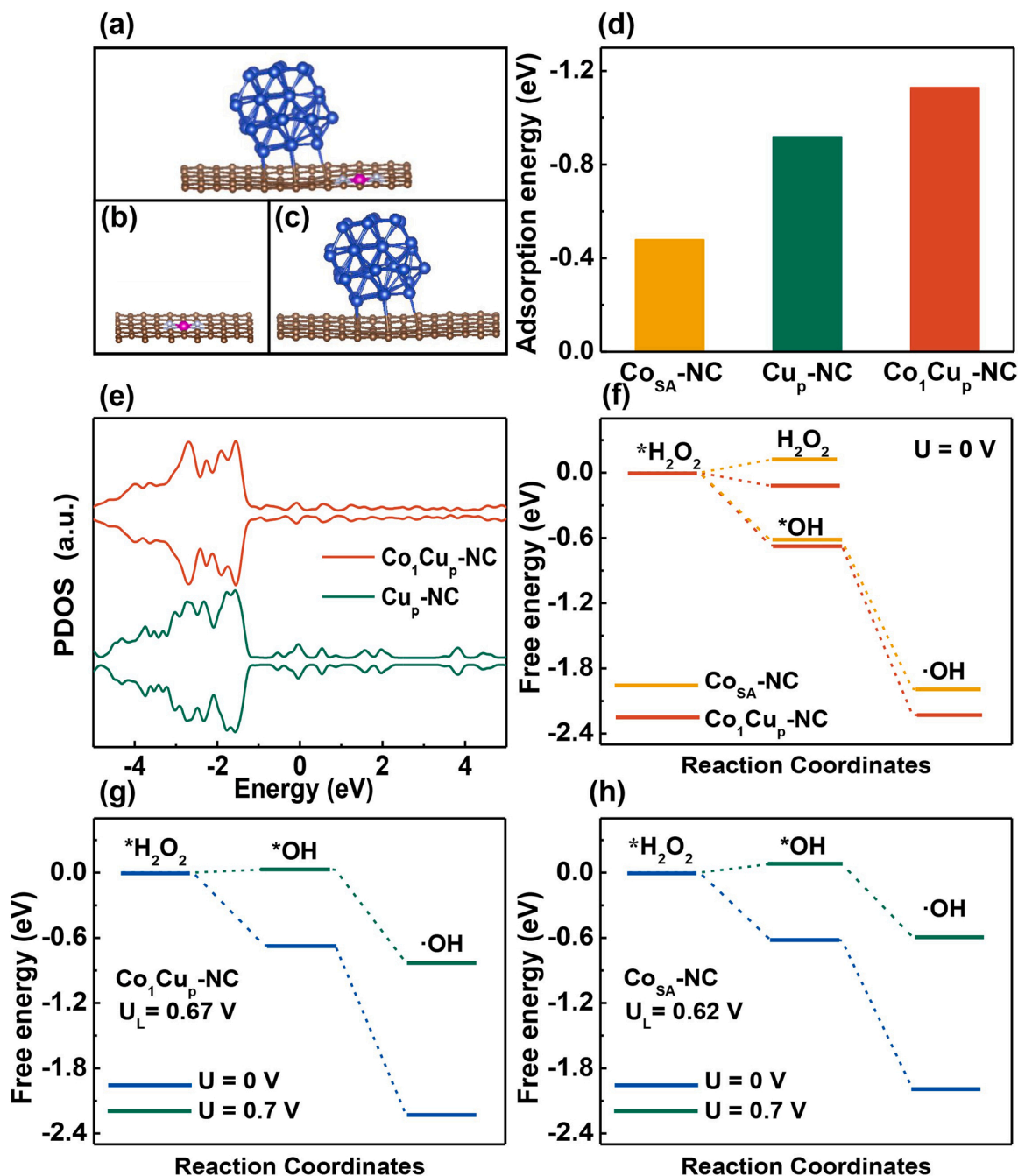


Fig. 6. Optimized structure models of (a) $\text{Co}_1\text{Cu}_p\text{-NC}$, (b) $\text{Co}_{\text{SA}}\text{-NC}$ and (c) $\text{Cu}_p\text{-NC}$. (d) Adsorption energy of the 2,4-D. (e) Projected density of states of Cu on the above systems. (f) The thermodynamic activity of H_2O_2 reduction and desorption. Free energy of H_2O_2 reduction on different catalysts: (g) $\text{Co}_1\text{Cu}_p\text{-NC}$ and (h) $\text{Co}_{\text{SA}}\text{-NC}$.

pyrrole-type CoN_4 was 0.06 eV for the reduction of O_2 to H_2O_2 by 2e^- ORR. After adsorbing H_2O_2 , it showed that high-spin pyrrole-type CoN_4 promoted the desorption of H_2O_2 [75]. In addition, Jung et al. have also reported that when electron-rich species (such as O^* and OH^*) were adsorbed near Co-N_4 , $\Delta G(\text{H}_2\text{O}_2)$ increased from 3.9 eV to very close to the optimal value of H_2O_2 production [76]. In present study, the energy barrier of H_2O_2 reduction activation on $\text{Co}_{\text{SA}}\text{-NC}$ and $\text{Co}_1\text{Cu}_p\text{-NC}$ were calculated. The reduction process of H_2O_2 on $\text{Co}_{\text{SA}}\text{-NC}$ and $\text{Co}_1\text{Cu}_p\text{-NC}$ was exothermic. The OH^* formation process $\Delta G = -1.99 \text{ eV}$ and -2.23 eV on $\text{Co}_{\text{SA}}\text{-NC}$ and $\text{Co}_1\text{Cu}_p\text{-NC}$ were much lower than 0.12 eV and -0.12 eV of $\Delta G(\text{H}_2\text{O}_2)$ formation process, indicating that H_2O_2 activation OH^* had more thermodynamic advantages.

Experimental and DFT calculation results showed that the excellent

2,4-D removal rate of $\text{Co}_1\text{Cu}_p\text{-NC}$ was due to the synergistic effect of electroreductive dechlorination and OH^* oxidation. Cluster Cu doping significantly improved the electroreductive dechlorination performance of 2,4-D, and single-atom Co doping significantly enhanced the 2e^- ORR activity and selectivity. In addition, single-atom Co doping promoted the interaction between cluster Cu and 2,4-D, which increased the adsorption energy and facilitates electron transfer. The highly unsaturated coordination of single atom Co could rapidly generate H_2O_2 . In addition, the cluster Cu around single-atom Co fine-tuned its electronic environment, which was more favorable for the generation and activation of H_2O_2 . Therefore, the enhanced degradation of 2,4-D at the $\text{Co}_1\text{Cu}_p\text{-NC}$ cathode was attributed to the synergistic effect of cluster Cu and single-atom Co. 2,4-D was preferentially adsorbed on Cu clusters, and the rapid

dechlorination of 2,4-D after adsorption benefited from the fast electron transfer ability. Meanwhile, due to the excellent $2e^-$ ORR activity and selectivity of single-atom Co, O_2 was adsorbed on single-atom Co, and the adsorbed O_2 was reduced to H_2O_2 . The adsorbed H_2O_2 was then continuously catalyzed to $\cdot OH$.

The above analyses established that the Co_1Cu_p -NC electrocatalytic system removed 2,4-D by DET and through the action of $\cdot OH$. Frontier molecular orbital theory was used to predict the most likely sites of attack on the 2,4-D molecule (the optimized structure of which is shown in Fig. S19a). Essentially, the highest occupied molecular orbital (HOMO) and the lowest unoccupied molecular orbital (LUMO) can describe the position where organic pollutant molecules are more likely to lose or obtain electrons during degradation. The HOMO and LUMO determined for the 2,4-D molecule are presented in Fig. S19b and c. The HOMO orbital indicates a site at which an electron is readily removed and so is susceptible to electrophilic attack while the LUMO orbital is related to nucleophilic reactions. It can be seen from Fig. S19b that the HOMO orbital was primarily located around the Cl7, O8 and Cl13 regions while the LUMO orbital was mainly situated on the benzene ring. These sites were therefore vulnerable to the attack of active substances during the degradation process.

In addition, the surface electrostatic potential (ESP) and average local ionization energy (ALIE) values for 2,4-D were calculated to predict the reaction sites. The ESP is composed of nuclear charge and electron density and is directly related to the electronic structure of a system. As such, this value is often used to predict electrophilic and nucleophilic reaction sites. Specifically, a region having a more negative ESP is more likely to attract an electrophilic species. Fig. S19d demonstrates that electrons were primarily concentrated at the Cl7 and Cl13 sites, and so these atoms were likely to undergo electrophilic attack. The ALIE value can be used to predict reaction sites based on the ionization energies of electrons at localized positions. A lower value suggests more weakly bound electrons and so identifies sites at which electrophilic or free radical reactions are likely to take place. The results in Fig. 6e show low values at Cl7 and Cl13 and so electrophilic or free radical reactions would be expected to occur at these sites.

These ESP and ALIE analyses established the sites on the 2,4-D molecule most likely to undergo reactions. These active sites were examined in more detail using the reduced condensed Fukui function (CFF) based on the Hirshfeld algorithm. As shown in Table S6, the atoms f^- (electrophilic attack), f^+ (nucleophilic attack) and f^0 (free radical attack) calculated by the CFF method represent the possibilities of electrophilic, nucleophilic, and radical attacks, respectively (Fig. S19 g and f). Larger Fukui function values are also associated with higher reactivity. The Cl7 and Cl13 sites were found to have higher f^- and f^0 values and so would likely be the main sites of electrophilic and free radical attack.

Based on the reaction products determined by mass spectrometry (Table S7), a possible pathway for 2,4-D degradation in the Co_1Cu_p -NC electrocatalytic system was devised and is presented in Fig. S20. The generation of low molecular weight compounds from 2,4-D is believed to have involved three reactions: hydroxylation, dechlorination and aromatic ring cleavage. Initially, a 2,4-D molecule is adsorbed on the catalyst surface where it undergoes preferential attack by electrons, cleaving a C-Cl bond to form o-chlorophenoxyacetic acid and p-chlorophenoxyacetic acid. This step releases chlorine free radicals that are then directly reduced on the cathode to generate chloride ions. Although there are two different possible dechlorination pathways, a much higher concentration of o-CPA was detected and so the para-chlorine atom was evidently eliminated more easily. The o-CPA and p-CPA subsequently undergo reduction reactions to produce PA that is then hydroxylated to give CP. This product, in turn, is hydroxylated to HQ and PBQ. The 2,4-D in the solution is also attacked by $\cdot OH$ radicals with cleavage of a C-O bond such that a $-OCH_2COOH$ groups is lost and 2,4-DCP and glycolic acid are produced. The glycolic acid is subsequently oxidized to CO_2 and H_2O by $\cdot OH$ while the 2,4-DCP is hydroxylated to 4-CC and 2-CHQ,

which are both then hydroxylated to BZ. Following this, the aromatic ring of the final hydroxylated product is destroyed by a decarboxylation reaction with free radicals to form small molecules such as oxalic, maleic, acetic, and formic acids, with eventual complete decomposition to produce CO_2 and H_2O . In order to further determine the degradation pathways, the intermediates were tested quantitatively. As shown in Figs. S21, 2,4-D was preferentially dechlorinated and all these intermediates increased with treatment time until they reached a peak, then were further broken down and almost completely removed within 80 min.

4. Conclusions

Atomic Co and Cu nanoclusters were applied to NC to produce electrochemical cathodes that promoted the reduction-oxidation heterogeneous electrocatalytic degradation of chlorinated organic pollutants. The mineralization of 2,4-D was achieved over this material and the degradation performance and mechanism were studied in detail. Various free radical scavenging experiments, quantitative analyses and electrochemical assessments demonstrated that $\cdot OH$ radicals and DET were responsible for the efficient decomposition of 2,4-D. DFT calculations indicated that electrons were rapidly transferred to 2,4-D through the Cu sites. The microelectronic environment around Co sites promoted the $2e^-$ ORR to increase performance and to activate H_2O_2 to generate $\cdot OH$ via a $1e^-$ process. The Co_1Cu_p -NC electrocatalytic system achieved complete dechlorination of 2,4-D and 93.4% TOC removal at 2 h and the reaction kinetics constant was $546.4 \text{ min}^{-1} \cdot g_{\text{metal}}^{-1}$, showing excellent organic pollutant degradation performance. The synergistic combination of DET and indirect oxidation by $\cdot OH$ promoted the remediation process, providing a means of dechlorination and mineralization. This work demonstrates a new strategy for the fabrication of highly active and multifunctional electrocatalysts for the treatment of chlorinated organic pollutants in water.

CRedit authorship contribution statement

Lu Liu: Conceptualization, Methodology, Investigation, Data curation, Formal analysis, Visualization, Writing – original draft. **Yiran Chen:** Data curation, Visualization. **Shunlin Li:** Formal analysis. **Wenchao Yu:** Methodology. **Xinyu Zhang:** Investigation. **Hui Wang:** Conceptualization, Supervision, Writing – review & editing, Funding acquisition, Project administration. **Jianan Ren:** Validation, Data curation. **Zhaoyong Bian:** Conceptualization, Supervision, Writing – review & editing, Funding acquisition.

Declaration of Competing Interest

The authors declare that they have no known competing financial interests or personal relationships that could have appeared to influence the work reported in this paper.

Data availability

Data will be made available on request.

Acknowledgments

This work was supported by the National Natural Science Foundation of China (No. 52270057 and 52070015), Beijing Natural Science Foundation of China (No. 8222061), and Beijing Forestry University Outstanding Young Talent Cultivation Project (No. 2019JQ03007).

Appendix A. Supporting information

Supplementary data associated with this article can be found in the online version at doi:10.1016/j.apcatb.2023.122748.

References

- [1] M.F. Jia, Z. Zhang, J.H. Li, H.J. Shao, L.X. Chen, X.B. Yang, A molecular imprinting fluorescence sensor based on quantum dots and a mesoporous structure for selective and sensitive detection of 2,4-dichlorophenoxyacetic acid, *Sens. Actuators B Chem.* 252 (2017) 934–943, <https://doi.org/10.1016/j.snb.2017.06.090>.
- [2] E.M. Frick, L.C. Strader, Roles for IBA-derived auxin in plant development, *J. Exp. Bot.* 69 (2017) 169–177, <https://doi.org/10.1093/jxb/erx298>.
- [3] N. Jaafarzadeh, F. Ghanbari, M. Ahmadi, Efficient degradation of 2,4-dichlorophenoxyacetic acid by peroxymonosulfate/magnetic copper ferrite nanoparticles/ozone: A novel combination of advanced oxidation processes, *Chem. Eng. J.* 320 (2017) 436–447, <https://doi.org/10.1016/j.cej.2017.03.036>.
- [4] M. Golshan, B. Kakavandi, M. Ahmadi, M. Azizi, Photocatalytic activation of peroxymonosulfate by TiO₂ anchored on copper ferrite (TiO₂@CuFe₂O₄) into 2,4-D degradation: Process feasibility mechanism and pathway, *J. Hazard. Mater.* 359 (2018) 325–337, <https://doi.org/10.1016/j.jhazmat.2018.06.069>.
- [5] M. Pera-Titus, V. Garcia-Molina, M.A. Baños, J. Giménez, S. Espluga, Degradation of chlorophenols by means of advanced oxidation processes: A general review, *Appl. Catal. B Environ.* 47 (2004) 219–256, <https://doi.org/10.1016/j.apcatb.2003.09.010>.
- [6] W.H. Zhang, Z.Y. Bian, Y.Y. Peng, H.Y. Tang, H. Wang, Dual-function oxygen vacancy of BiOBr intensifies pollutant adsorption and molecular oxygen activation to remove tetracycline hydrochloride, *Chem. Eng. J.* 451 (2023), 138731, <https://doi.org/10.1016/j.cej.2022.138731>.
- [7] B.Q. Gao, Y. Pan, H. Yang, Enhanced photo-Fenton degradation of fluoroquinolones in water assisted by a 3D composite sponge complexed with a S-scheme MoS₂/Bi₂S₃/BiVO₄ ternary photocatalyst, *Appl. Catal. B Environ.* 315 (2022), 121580, <https://doi.org/10.1016/j.apcatb.2022.121580>.
- [8] M. Li, Y.T. Jin, D.Y. Cao, L.L. Yang, J.F. Yan, Z.X. Zhang, Z. Liu, L.W. Huang, S. Q. Zhou, J.L. Cheng, Q. Zhao, H.M. Zhao, N.X. Feng, C.H. Mo, Efficient decomposition of perfluorooctane sulfonate by electrochemical activation of peroxymonosulfate in aqueous solution: Efficacy reaction mechanism active sites and application potential, *Water Res.* 221 (2022), 118778, <https://doi.org/10.1016/j.watres.2022.118778>.
- [9] Z. Luo, M. Liu, D. Tang, Y. Xu, H. Han, J. He, K. Chen, J. Sun, High H₂O₂ selectivity and enhanced Fe²⁺ regeneration toward an effective electro-Fenton process based on a self-doped porous biochar cathode, *Appl. Catal. B Environ.* 315 (2022), 121523, <https://doi.org/10.1016/j.apcatb.2022.121523>.
- [10] C. Zhang, Y. Li, H.C. Shen, D.M. Shuai, Simultaneous coupling of photocatalytic and biological processes: A promising synergistic alternative for enhancing decontamination of recalcitrant compounds in water, *Chem. Eng. J.* 403 (2021), 126365, <https://doi.org/10.1016/j.cej.2020.126365>.
- [11] X.D. Zhang, J. Wang, B.B. Xiao, Y.J. Pu, Y.C. Yang, J.S. Geng, D.Y. Wang, X. J. Chen, Y.X. Wei, K. Xiong, Y.F. Zhu, Resin-based photo-self-Fenton system with intensive mineralization by the synergistic effect of holes and hydroxyl radicals, *Appl. Catal. B Environ.* 315 (2022), 121525, <https://doi.org/10.1016/j.apcatb.2022.121525>.
- [12] K. Zhao, X. Quan, Y. Su, X. Qin, S. Chen, H.T. Yu, Enhanced chlorinated pollutant degradation by the synergistic effect between dechlorination and hydroxyl radical oxidation on a bimetallic single-atom catalyst, *Environ. Sci. Technol.* 55 (2021) 14194–14203, <https://doi.org/10.1021/acs.est.1c04943>.
- [13] E. Brillas, C.A. Martínez-Huitle, Decontamination of wastewaters containing synthetic organic dyes by electrochemical methods. An updated review, *Appl. Catal. B Environ.* 166–167 (2015) 603–643, <https://doi.org/10.1016/j.apcatb.2014.11.016>.
- [14] S.O. Ganiyu, M. Zhou, C.A. Martínez-Huitle, Heterogeneous electro-Fenton and photoelectro-Fenton processes: A critical review of fundamental principles and application for water/wastewater treatment, *Appl. Catal. B Environ.* 235 (2018) 103–129, <https://doi.org/10.1016/j.apcatb.2018.04.044>.
- [15] Y.J. Yang, Z.Y. Bian, L. Zhang, H. Wang, Bi@Bio(OH)_y modified oxidized g-C₃N₄ photocatalytic removal of tetracycline hydrochloride with highly effective oxygen activation, *J. Hazard. Mater.* 427 (2022), 127866, <https://doi.org/10.1016/j.jhazmat.2021.127866>.
- [16] L. Zhang, X.Y. Zhang, C. Wei, F. Wang, H. Wang, Z.Y. Bian, Interface engineering of Z-scheme α-Fe₂O₃/g-C₃N₄ photoanode: Simultaneous enhancement of charge separation and hole transportation for photoelectrocatalytic organic pollutant degradation, *Chem. Eng. J.* 435 (2022), 134873, <https://doi.org/10.1016/j.cej.2022.134873>.
- [17] Y.J. Yang, Z.Y. Bian, Oxygen doping through oxidation causes the main active substance in g-C₃N₄ photocatalysis to change from holes to singlet oxygen, *Sci. Total Environ.* 753 (2021), 141908, <https://doi.org/10.1016/j.scitotenv.2020.141908>.
- [18] W.H. Zhang, Y.Y. Peng, Y.J. Yang, L. Zhang, Z.Y. Bian, H. Wang, Bismuth-rich strategy intensifies the molecular oxygen activation and internal electrical field for the photocatalytic degradation of tetracycline hydrochloride, *Chem. Eng. J.* 430 (2022), 132963, <https://doi.org/10.1016/j.cej.2021.132963>.
- [19] Z.M. Lou, C.C. Yu, X.F. Wen, Y.H. Xu, J.M. Yu, X.H. Xu, Construction of Pd nanoparticles/two-dimensional Co-MOF nanosheets heterojunction for enhanced electrocatalytic hydrodechlorination, *Appl. Catal. B Environ.* 317 (2022), 121730, <https://doi.org/10.1016/j.apcatb.2022.121730>.
- [20] Y.Y. Ren, Y.S. Yang, L.F. Chen, L. Wang, Y.W. Shi, P. Yin, W.L. Wang, M.F. Shao, X. Zhang, M. Wei, Synergistic effect of Cu⁰/Cu⁺ derived from layered double hydroxides toward catalytic transfer hydrogenation reaction, *Appl. Catal. B Environ.* 314 (2022), 121515, <https://doi.org/10.1016/j.apcatb.2022.121515>.
- [21] J.F. Kou, W.D. Wang, J. Fang, F. Li, H.C. Zhao, J.F. Li, H.H. Zhu, B.Y. Li, Z.P. Dong, Precisely controlled Pd nanoclusters confined in porous organic cages for size-dependent catalytic hydrogenation, *Appl. Catal. B Environ.* 315 (2022), 121487, <https://doi.org/10.1016/j.apcatb.2022.121487>.
- [22] Y.Z. Song, H.Y. Tang, Y.J. Yan, Y.J. Guo, H. Wang, Z.Y. Bian, Combining electrokinetic treatment with modified zero-valent iron nanoparticles for rapid and thorough dechlorination of trichloroethene, *Chemosphere* 292 (2022), 133443, <https://doi.org/10.1016/j.chemosphere.2021.133443>.
- [23] D.D. Zhang, Y.Y. Peng, L. Zhang, Y.J. Guo, L. Liu, H. Wang, Z.Y. Bian, Synergistic effect of atomically dispersed Fe-Ni pair sites for electrocatalytic reactions to remove chlorinated organic compounds, *Chemosphere* 303 (2022), 134992, <https://doi.org/10.1016/j.chemosphere.2022.134992>.
- [24] H.J. Qin, T.J. Zha, K. Qian, Y.K. Sun, X.H. Guan, C.C. Chen, Efficient full dechlorination of chlorinated ethenes on single enzyme-like Co-N₄ sites in nitrogen-doped carbons, *Appl. Catal. B Environ.* 328 (2023), 122459, <https://doi.org/10.1016/j.apcatb.2023.122459>.
- [25] H.D. Li, M.Z. Sun, Y. Pan, J. Xiong, H.Y. Du, Y.D. Yu, S.H. Feng, Z.J. Li, J.P. Lai, B. L. Huang, The self-complementary effect through strong orbital coupling in ultrathin high-entropy alloy nanowires boosting pH-universal multifunctional electrocatalysis, *Appl. Catal. B Environ.* 312 (2022), 121431, <https://doi.org/10.1016/j.apcatb.2022.121431>.
- [26] X.Q. Shen, F. Xiao, H.Y. Zhao, Y. Chen, C. Fang, R. Xiao, W.H. Chu, G.H. Zhao, In situ-formed PdFe nanoalloy and carbon defects in cathode for synergic reduction-oxidation of chlorinated pollutants in electro-Fenton process, *Environ. Sci. Technol.* 54 (2020) 4564–4572, <https://doi.org/10.1021/acs.est.9b05896>.
- [27] N. Li, X.Z. Song, L. Wang, X.L. Geng, H. Wang, H.Y. Tang, Z.Y. Bian, Single-atom cobalt catalysts for electrocatalytic hydrodechlorination and oxygen reduction reaction for the degradation of chlorinated organic compounds, *ACS Appl. Mater. Interfaces* 12 (2020) 24019–24029, <https://doi.org/10.1021/acsami.0c05159>.
- [28] X. Qin, P.K. Cao, X. Quan, K. Zhao, S. Chen, H.T. Yu, Y. Su, Highly efficient hydroxyl radicals production boosted by the atomically dispersed Fe and Co sites for heterogeneous electro-Fenton oxidation, *Environ. Sci. Technol.* 57 (2023) 2907–2917, <https://doi.org/10.1021/acs.est.2c06981>.
- [29] X.Z. Song, N. Li, H. Zhang, L. Wang, Y.J. Yan, H. Wang, L.Y. Wang, Z.Y. Bian, Graphene-supported single nickel atom catalyst for highly selective and efficient hydrogen peroxide production, *ACS Appl. Mater. Interfaces* 12 (2020) 17519–17527, <https://doi.org/10.1021/acsami.0c01278>.
- [30] X.Z. Song, H. Zhang, Z.Y. Bian, H. Wang, In situ electrogeneration and activation of H₂O₂ by atomic Fe catalysts for the efficient removal of chloramphenicol, *J. Hazard. Mater.* 412 (2021), 125162, <https://doi.org/10.1016/j.jhazmat.2021.125162>.
- [31] Y.N. Ding, W. Zhou, J.H. Gao, F. Sun, G.B. Zhao, H₂O₂ electrogeneration from O₂ electroreduction by N-doped carbon materials: A mini-review on preparation methods selectivity of N sites and prospects, *Adv. Mater. Interfaces* 8 (2021), <https://doi.org/10.1002/admi.202002091>.
- [32] Y.F. Bu, Y.B. Wang, G.F. Han, Y.X. Zhao, X.L. Ge, F. Li, Z.H. Zhang, Q. Zhong, J. B. Baek, Carbon-based electrocatalysts for efficient hydrogen peroxide production, *Adv. Mater.* 33 (2021), e2103266, <https://doi.org/10.1002/adma.202103266>.
- [33] Y.Y. Sun, L. Silviali, N.R. Sahraie, W. Ju, J.K. Li, A. Zitolo, S. Li, A. Bagger, L. Arnanson, X.L. Wang, T. Moeller, D. Bernsmeier, J. Rossmeisl, F. Jaouen, P. Strasser, Activity-selectivity trends in the electrochemical production of hydrogen peroxide over single-site metal-nitrogen-carbon catalysts, *J. Am. Chem. Soc.* 141 (2019) 12372–12381, <https://doi.org/10.1021/jacs.9b05576>.
- [34] C. Tang, L. Chen, H.J. Li, L.Q. Li, Y. Jiao, Y. Zheng, H.L. Xu, K. Davey, S.Z. Qiao, Tailoring acidic oxygen reduction selectivity on single-atom catalysts via modification of first and second coordination spheres, *J. Am. Chem. Soc.* 143 (2021) 7819–7827, <https://doi.org/10.1021/jacs.1c03135>.
- [35] C. Liu, H. Li, F. Liu, J.S. Chen, Z.X. Yu, Z.W. Yuan, C.J. Wang, H.L. Zheng, G. Henkelman, L. Wei, Y. Chen, Intrinsic activity of metal centers in metal-nitrogen-carbon single-atom catalysts for hydrogen peroxide synthesis, *J. Am. Chem. Soc.* 142 (2020) 21861–21871, <https://doi.org/10.1021/jacs.0c10636>.
- [36] W. Liu, C. Zhang, J.G. Zhang, X. Huang, M. Song, J.W. Li, F. He, H.P. Yang, J. Zhang, D. Wang, Tuning the atomic configuration of Co-N-C electrocatalyst enables highly-selective H₂O₂ production in acidic media, *Appl. Catal. B Environ.* 310 (2022), 121312, <https://doi.org/10.1016/j.apcatb.2022.121312>.
- [37] T. Gu, H.X. Dong, T.L. Lu, L. Han, Y.Z. Zhan, Fluoride ion accelerating degradation of organic pollutants by Cu(II)-catalyzed Fenton-like reaction at wide pH range, *J. Hazard. Mater.* 377 (2019) 365–370, <https://doi.org/10.1016/j.jhazmat.2019.05.073>.
- [38] J.J. Long, L.Q. Xu, L.H. Zhao, H.Q. Chu, Y.F. Mao, D. Wu, Activation of dissolved molecular oxygen by Cu(0) for bisphenol A degradation: Role of Cu(0) and formation of reactive oxygen species, *Chemosphere* 241 (2020), 125034, <https://doi.org/10.1016/j.chemosphere.2019.125034>.
- [39] L. Lyu, W.R. Cao, G.F. Yu, D.B. Yan, K.L. Deng, C. Lu, C. Hu, Enhanced polarization of electron-poor/rich micro-centers over nZVCu-Cu(II)-rGO for pollutant removal with H₂O₂, *J. Hazard. Mater.* 383 (2020), 121182, <https://doi.org/10.1016/j.jhazmat.2019.121182>.
- [40] Y.F. Sun, L.Y. Shen, Q. Qin, L.W. Jiang, Y.Q. Su, Y.L. Wang, L.G. Xia, S.L. Lin, W. F. Yao, Q. Wu, Q.J. Xu, Enhanced reactive oxygen species via in situ producing H₂O₂ and synchronous catalytic conversion at stable modified copper foam cathode for efficient high-concentration organic wastewater treatment and simultaneous electricity generation, *Chemosphere* 291 (2022), 132911, <https://doi.org/10.1016/j.chemosphere.2021.132911>.
- [41] R. Mao, C. Huang, X. Zhao, M. Ma, J.H. Qu, Dechlorination of triclosan by enhanced atomic hydrogen-mediated electrochemical reduction: Kinetics mechanism and toxicity assessment, *Appl. Catal. B Environ.* 241 (2019) 120–129, <https://doi.org/10.1016/j.apcatb.2018.09.013>.

- [42] R. Mao, N. Li, H.C. Lan, X. Zhao, H.J. Liu, J.H. Qu, M. Sun, Dechlorination of trichloroacetic acid using a noble metal-free graphene-Cu foam electrode via direct cathodic reduction and atomic H^{*}, *Environ. Sci. Technol.* 50 (2016) 3829–3837, <https://doi.org/10.1021/acs.est.5b05006>.
- [43] J.J. Gao, H.B. Yang, X. Huang, S.F. Hung, W.Z. Cai, C.M. Jia, S. Miao, H.M. Chen, X.F. Yang, Y.Q. Huang, T. Zhang, B. Liu, Enabling direct H₂O₂ production in acidic media through rational design of transition metal single atom catalyst, *Chem* 6 (2020) 658–674, <https://doi.org/10.1016/j.chempr.2019.12.008>.
- [44] X.Z. Song, N. Li, H. Zhang, L. Wang, Y.J. Yan, H. Wang, L.Y. Wang, Z.Y. Bian, Graphene-supported single nickel atom catalyst for highly selective and efficient hydrogen peroxide production, *ACS Appl. Mater. Interfaces* 12 (2020) 17519–17527, <https://doi.org/10.1021/acsami.0c01278>.
- [45] G. Kresse, J. Furthmüller, Efficiency of ab-initio total energy calculations for metals and semiconductors using a plane-wave basis set, *Comput. Mater. Sci.* 6 (1996) 15–50, [https://doi.org/10.1016/0927-0256\(96\)00008-0](https://doi.org/10.1016/0927-0256(96)00008-0).
- [46] G. Kresse, J. Furthmüller, Efficient iterative schemes for ab initio total-energy calculations using a plane-wave basis set, *Phys. Rev. B Condens. Matter* 54 (1996) 11169–11186, <https://doi.org/10.1103/PhysRevB.54.11169>.
- [47] T. Lu, Q.X. Chen, Realization of conceptual density functional theory and information-theoretic approach in multiwfn program, *Concept. Density Funct. Theory* 2 (2022) 631–647, <https://doi.org/10.1002/9783527829941.ch31>.
- [48] T. Lu, F.W. Chen, Multiwfn: A multifunctional wavefunction analyzer, *J. Comput. Chem.* 33 (2012) 580–592, <https://doi.org/10.1002/jcc.22885>.
- [49] M. Mantina, A.C. Chamberlin, R. Valero, C.J. Cramer, D.G. Truhlar, Consistent van der Waals radii for the whole main group, *J. Phys. Chem. A* 113 (2009) 5806–5812, <https://doi.org/10.1021/jp8111556>.
- [50] H.X. Yao, X.K. Wang, K. Li, C. Li, C.H. Zhang, J. Zhou, Z.W. Cao, H.L. Wang, M. Gu, M.H. Huang, H.Q. Jiang, Strong electronic coupling between ruthenium single atoms and ultrafine nanoclusters enables economical and effective hydrogen production, *Appl. Catal. B Environ.* 312 (2022), 121378, <https://doi.org/10.1016/j.apcatb.2022.121378>.
- [51] X. Wan, Q.T. Liu, J.Y. Liu, S.Y. Liu, X.F. Liu, L.Z. Zheng, J.X. Shang, R.H. Yu, J. L. Shui, Iron atom-cluster interactions increase activity and improve durability in Fe-N-C fuel cells, *Nat. Commun.* 13 (2022) 2963, <https://doi.org/10.1038/s41467-022-30702-z>.
- [52] X.M. Peng, J.Q. Wu, Z.L. Zhao, X. Wang, H.L. Dai, Y. Wei, G.P. Xu, F.P. Hu, Activation of peroxymonosulfate by single atom Co-N-C catalysts for high-efficient removal of chloroquine phosphate via non-radical pathways: Electron-transfer mechanism, *Chem. Eng. J.* 429 (2022), 132245, <https://doi.org/10.1016/j.cej.2021.132245>.
- [53] M. Ahmad, S. Chen, F. Ye, X. Quan, S. Afzal, H. Yu, X. Zhao, Efficient photo-Fenton activity in mesoporous MIL-100(Fe) decorated with ZnO nanosphere for pollutants degradation, *Appl. Catal. B Environ.* 245 (2019) 428–438, <https://doi.org/10.1016/j.apcatb.2018.12.057>.
- [54] C.Z. Zhu, Q.R. Shi, B.Z. Xu, S.F. Fu, G. Wan, C. Yang, S.Y. Yao, J.H. Song, H. Zhou, D. Du, S.P. Beckman, D. Su, Y.H. Lin, Hierarchically porous M-N-C (M = Co and Fe) single-atom electrocatalysts with robust MN_x active moieties enable enhanced ORR performance, *Adv. Energy Mater.* 8 (2018) 1801956, <https://doi.org/10.1002/aenm.201801956>.
- [55] S.Z. Song, T. Qin, Q. Li, Y.Q. Wang, Y.F. Tang, L.F. Zhang, X.J. Liu, Single Co atoms implanted into N-doped hollow carbon nanoshells with Non-Planar Co-N₄-1-O₂ sites for efficient oxygen electrochemistry, *Inorg. Chem.* 60 (2021) 7498–7509, <https://doi.org/10.1021/acs.inorgchem.1c00824>.
- [56] N.Q. Zhang, Y.Q. Yi, J.T. Lian, Z.Q. Fang, Effects of Ce doping on the Fenton-like reactivity of Cu-based catalyst to the fluconazole, *Chem. Eng. J.* 395 (2020), 124897, <https://doi.org/10.1016/j.cej.2020.124897>.
- [57] Y.F. Song, J.R.C. Junqueira, N. Sikdar, D. Ohl, S. Dieckhofer, T. Quast, S. Seisel, J. Masa, C. Andronesco, W. Schuhmann, B-Cu-Zn gas diffusion electrodes for CO₂ electroreduction to C₂₊ products at high current densities, *Angew. Chem. Int. Ed.* 60 (2021) 9135–9141, <https://doi.org/10.1002/anie.202016898>.
- [58] H.J. Shen, N.X. Qiu, L. Yang, X.Y. Guo, K. Zhang, T.J. Thomas, S.Y. Du, Q.F. Zheng, J.P. Attfield, Y. Zhu, M.H. Yang, Boosting oxygen reduction for high-efficiency H₂O₂ electrosynthesis on oxygen-coordinated Co-N-C catalysts, *Small* 18 (2022), e2200730, <https://doi.org/10.1002/sml.202200730>.
- [59] Q.R. Zhang, X. Tan, N.M. Bedford, Z.J. Han, L. Thomsen, S. Smith, R. Amal, X. Y. Lu, Direct insights into the role of epoxy groups on cobalt sites for acidic H₂O₂ production, *Nat. Commun.* 11 (2020) 4181, <https://doi.org/10.1038/s41467-020-17782-5>.
- [60] G.F. Chen, O.A. Syzgantseva, M.A. Syzgantseva, S.L. Yang, G.H. Yan, L. Peng, C. Y. Cao, W.X. Chen, Z.W. Wang, F.J. Qin, T.Z. Lei, X.H. Zeng, L. Lin, W.G. Song, B. X. Han, Construction of synergistic Co and Cu diatomic sites for enhanced higher alcohol synthesis, *CCS Chem.* (2022) 1–14, <https://doi.org/10.31635/ccschem.022.202201930>.
- [61] I.A. Pankin, A. Martini, K.A. Lomachenko, A.V. Soldatov, S. Bordiga, E. Borfecchia, Identifying Cu-oxo species in Cu-zeolites by XAS: A theoretical survey by DFT-assisted XANES simulation and EXAFS wavelet transform, *Catal. Today* 345 (2020) 125–135, <https://doi.org/10.1016/j.cattod.2019.09.032>.
- [62] J.D. Yi, X.P. Gao, H. Zhou, W. Chen, Y. Wu, Design of Co-Cu diatomic site catalysts for high-efficiency synergistic CO₂ electroreduction at industrial-level current density, *Angew. Chem.* 134 (2022), e202212329, <https://doi.org/10.1002/ange.202212329>.
- [63] J.L. Wang, S.Z. Wang, Effect of inorganic anions on the performance of advanced oxidation processes for degradation of organic contaminants, *Chem. Eng. J.* 411 (2021), 128392, <https://doi.org/10.1016/j.cej.2020.128392>.
- [64] L. Wang, J.H. Lu, L. Li, Y.Y. Wang, Q.G. Huang, Effects of chloride on electrochemical degradation of perfluorooctanesulfonate by magnéli phase Ti₄O₇ and boron doped diamond anodes, *Water Res.* 170 (2020), 115254, <https://doi.org/10.1016/j.watres.2019.115254>.
- [65] K.X. Wang, D.H. Huang, W.L. Wang, Y.Y. Ji, J.F. Niu, Enhanced perfluorooctanoic acid degradation by electrochemical activation of peroxymonosulfate in aqueous solution, *Environ. Int.* 137 (2020), 105562, <https://doi.org/10.1016/j.envint.2020.105562>.
- [66] Z. Liu, H.J. Ding, C. Zhao, T. Wang, P. Wang, D.D. Dionysiou, Electrochemical activation of peroxymonosulfate with ACF cathode: Kinetics influencing factors mechanism and application potential, *Water Res.* 159 (2019) 111–121, <https://doi.org/10.1016/j.watres.2019.04.052>.
- [67] Y.Z. Zhang, X. Chen, C. Liang, L.F. Yin, Y. Yang, Reconstructing the coordination environment of single atomic Fe-catalysts for boosting the Fenton-like degradation activities, *Appl. Catal. B Environ.* 315 (2022), 121536, <https://doi.org/10.1016/j.apcatb.2022.121536>.
- [68] H. Chi, W. Jin, J. Zhang, Y. Xiu, T. Xu, Enhancement on the degradation of naproxen in Cu(0) activated peroxymonosulfate system by complexing reagents, *J. Hazard. Mater.* 437 (2022), 129416, <https://doi.org/10.1016/j.jhazmat.2022.129416>.
- [69] J.L. Wang, S.Z. Wang, Reactive species in advanced oxidation processes: Formation identification and reaction mechanism, *Chem. Eng. J.* 401 (2020), 126158, <https://doi.org/10.1016/j.cej.2020.126158>.
- [70] L.W. Chen, X.C. Li, J. Zhang, J.Y. Fang, Y.M. Huang, P. Wang, J. Ma, Production of hydroxyl radical via the activation of hydrogen peroxide by hydroxylamine, *Environ. Sci. Technol.* 49 (2015) 10373–10379, <https://doi.org/10.1021/acs.est.5b00483>.
- [71] K. Zhao, X. Quan, Y. Su, X. Qin, S. Chen, H.T. Yu, Enhanced chlorinated pollutant degradation by the synergistic effect between dechlorination and hydroxyl radical oxidation on a bimetallic single-atom catalyst, *Environ. Sci. Technol.* 55 (2021) 14194–14203, <https://doi.org/10.1021/acs.est.1c04943>.
- [72] L. Wang, H.F. Zeng, X. Yu, Dechlorination and decomposition of trichloroacetic acid by glow discharge plasma in aqueous solution, *Electrochim. Acta* 115 (2014) 332–336, <https://doi.org/10.1016/j.electacta.2013.10.160>.
- [73] F. Xiao, Z.N. Wang, J.Q. Fan, T. Majima, H.Y. Zhao, G.H. Zhao, Selective electrocatalytic reduction of oxygen to hydroxyl radicals via 3-electron pathway with FeCo alloy encapsulated carbon aerogel for fast and complete removing pollutants, *Angew. Chem. Int. Ed.* 60 (2021) 10375–10383, <https://doi.org/10.1002/anie.202101804>.
- [74] L.Z. Zhang, Y. Jia, G.P. Gao, X.C. Yan, N. Chen, J. Chen, M.T. Soo, B. Wood, D. J. Yang, A.J. Du, X.D. Yao, Graphene defects trap atomic Ni species for hydrogen and oxygen evolution reactions, *Chem* 4 (2018) 285–297, <https://doi.org/10.1016/j.chempr.2017.12.005>.
- [75] S.Y. Chen, T. Luo, X.Q. Li, K.J. Chen, J.W. Fu, K. Liu, C. Cai, Q.Y. Wang, H.M. Li, Y. Chen, C. Ma, L. Zhu, Y.R. Lu, T.S. Chan, M.S. Zhu, E. Cortés, M. Liu, Identification of the highly active Co-N₄ coordination motif for selective oxygen reduction to hydrogen peroxide, *J. Am. Chem. Soc.* 144 (2022) 14505–14516, <https://doi.org/10.1021/jacs.2c01194>.
- [76] E.Y. Jung, H.J. Shin, B.H. Lee, V. Efremov, S. Lee, H.S. Lee, J. Kim, W.H. Antink, S. Park, K.S. Lee, S.P. Cho, J.S. Yoo, Y.E. Sung, T. Hyeon, Atomic-level tuning of Co-N-C catalyst for high-performance electrochemical H₂O₂ production, *Nat. Mater.* 19 (2020) 436–442, <https://doi.org/10.1038/s41563-019-0571-5>.